Analytical theory of elastic electron backscattering from elements, alloys and compounds: Comparison with experimental data

A. Jablonski*

Institute of Physical Chemistry, Polish Academy of Sciences, ul. Kasprzaka 44/52, 01-224 Warsaw, Poland

(e-mail: ajablonski@ichf.edu.pl)

Abstract

Probability of elastic electron backscattering from surfaces is typically calculated from theoretical models implemented in Monte Carlo simulation strategies since this approach is considered to be the most accurate. However, an analytical model proposed by Oswald et al. [J. Electron Spectrosc. Relat. Phenom. 61 (1993) 251], after later modifications, has been found to be of similar accuracy. The relevant analysis was performed for selected elemental solids. In the present work, a possibility to use the analytical formalism in elastic peak electron spectroscopy for determination of the IMFP has been presently studied. For this purpose, two further modifications of the analytical theory were made: (i) creation of a database of parameters facilitating calculations of the angular distribution of electrons after multiple collisions, and (ii) extension of the formalism to solids constituted of different atomic species, i.e. alloys and compounds. Comparison of experimental data (angular distribution of backscattered electrons, ratios of elastic peak intensities) with predictions of both theoretical models proves that these models are of similar accuracy. The IMFPs for elemental solids derived from experimentally measured ratios using the analytical formalism

and the Monte Carlo simulations are practically identical. On analysis of IMFPs obtained for 13 elemental solids in the energy range from 200 eV to 5000 eV, it has been estimated that the IMFPs obtained from the analytical formalism deviate on average from IMFPs from Monte Carlo calculations by 3.09%. Similar agreement was found for an alloy ($Al_{0.48}Ni_{0.52}$) and compounds (GaSb, InSb, GaN and SiC) considered here.

Keywords: Elastic electron backscattering; inelastic mean free path; theory of electron transport; Monte Carlo simulations.

1. Introduction

Much interest in the phenomenon of elastic electron backscattering from solid surfaces is observed in the literature. One of the factors stimulating this interest is due to analytical applications of this effect [1,2]. These analytical methods have a high surface sensitivity [3] which results from the fact that the signal electrons pass a surface region twice. The analytical applications are based on theoretical models that describe the elastically backscattered electrons, e.g. the angular and energy distribution of backscattered current. The Monte Carlo simulations of electron transport in the surface region are frequently applied in relevant calculations since the theoretical model implemented in typical simulation strategies is the most realistic [4-10]. However, this approach is computationally expensive and, consequently, an analysis of a large volume of experimental data may be a rather slow procedure. It is expected that an analytical approach that describes phenomenon of elastic backscattering would be much faster. This expectation has stimulated a number of approaches to develop a relevant analytical formalism [4,8,10,11,17].

Derivation of an analytical formalism involves certain assumptions that simplify the theoretical model of electron transport. Consequently, the calculated characteristics of elastically backscattered electrons (angular distribution, electron energy dependence, etc.) may differ from results obtained from Monte Carlo simulations. Furthermore, the analytical theoretical models differ in complexity of the derived formalism and convenience to develop an effective algorithm. Possible applications of this formalism to process the experimental data require a compromise between accuracy of an analytical model and computational intricacies. To estimate accuracy of different analytical models, the Monte Carlo simulations can be used. Results of such analyses were published in the literature [8,10].

It follows from a recent analysis [10] that the model of Oswald et al. [11] after modification by Dubus et al. [8] has accuracy practically reaching the accuracy of Monte Carlo simulations. It has been found that ratios of elastic backscattering probabilities calculated for elemental solids from the analytical model and from the Monte Carlo simulations for typical experimental geometries differ on average by 3.14 %. Such deviation is comparable to statistical error of Monte Carlo simulations, or to the systematic deviation due to different Monte Carlo strategies. This analysis has been performed for 9 solids and for energies ranging from 200 eV to 5000 eV, i.e. in the energy range of interest for surface sensitive electron spectroscopies.

It has been postulated [10] that the modified analytical formalism is a prospective basis for analytical applications of the elastic backscattering effect. These applications are known under an acronym EPES (elastic peak electron spectroscopy) [1,2]. Unfortunately, the modified theory of Oswald et al. [8,11], despite apparent simplicity, is rather inconvenient in use due to problems in calculations of some of the needed parameters. Furthermore, the relevant formalism has been developed and tested for elemental solids. In analytical practice of EPES, we need a theoretical tool that applies to more complicated solids, e.g., alloys or

compounds. Furthermore, the extension of the analytical formalism to compounds needs a convincing support by extensive comparisons with experimental observations. All the above issues are presently addressed.

2. Theory

2.1. Analytical formalism for elemental solids

In practical EPES applications, we are interested in theoretical description of an elastic backscattering probability, η, into a solid angle, $\Delta\Omega$, of an analyzer. The relevant experimental configuration and the notation used here are shown in Fig. 1. According to modified theory of Oswald et al. [8,11], this probability per unity of a small solid angle is given by

$$d\eta / d\Omega = \frac{\mu}{\mu + \mu_0} \sum_{k=1}^{\infty} \frac{s^k}{k} H_k(\theta) \tag{1}$$

where $H_k(\theta)$ is the distribution of scattering angles, θ, after *k* elastic collisions, $\mu_0 = \cos\theta_0$, and $\mu = \cos\alpha$. The distribution $H_k(\theta)$ can be calculated from the relation [8,10,11,17]

$$H_k(\theta) = \frac{1}{2\pi} \sum_{l=0}^{\infty} \frac{2l+1}{2} (A_l)^k \; P_l(\cos\theta) \tag{2}$$

where $P_l(\cos\theta)$ are the Legendre polynomials,

$$A_l = \frac{2\pi}{\sigma_{el}} \int_0^{\pi} \frac{d\sigma_{el}}{d\Omega} P_l(\cos\theta) \sin\theta \, d\theta, \tag{3}$$

$d\sigma_{el} / d\Omega$ is the differential elastic scattering cross section, and σ_{el} is the total elastic scattering cross section

$$\sigma_{el} = \int_{4\pi} (d\sigma_{el} / d\Omega) \, d\Omega = 2\pi \int_0^{\pi} \frac{d\sigma_{el}}{d\Omega} \sin\theta \, d\theta \tag{4}$$

Parameter *s* in Eq. (1) comprises the elastic and inelastic scattering properties of a solid

$$s = \frac{\lambda_{in}}{\lambda_{in} + \lambda_{el}} \tag{5}$$

where λ_{in} is the electron inelastic mean free path, and λ_{el} is the elastic mean free path. The latter parameter for an elemental solid is given by

$$\lambda_{el} = \left(N\sigma_{el}\right)^{-1} \tag{6}$$

where *N* is the atomic density (number of atoms in a unit volume) and σ_{el} is the total elastic scattering cross section. Finally, the atomic density for an elemental solid can be estimated from the following relation typically used in the formalism of electron probe microanalysis [18]

$$N = N_A \rho / M \tag{7}$$

where N_A is the Avogadro number, ρ is the density, and *M* is the corresponding atomic mass.

Thus, to calculate the elastic electron backscattering probability, we need to know parameters describing the experimental configuration (angles θ_0, α, and $\Delta\alpha$) and the parameters describing the solid ($d\sigma_{el}/d\Omega$, λ_{in}, σ, *M*). Derivation of the above formalism [Eqs (1) – (5)] is based on the following assumptions [8,10,11]:

1) Only one large angle scattering event occurs along the trajectory of an electron entering the analyzer. Remaining scattering angles after elastic collisions are assumed to be very small and they are supposed not to affect the trajectory.

2) If *k* scattering events occur along the trajectory, all these events are taken into account in calculations of the angular distribution of electron directions with respect to the initial direction.

Example of a trajectory backscattered electron is outlined in Fig. 2. We see that specification of the depth of the scattering event, *z*, defines the trajectory shape and length which certainly

simplifies the derivation. Despite of this simplification, Eq. (1) has been found to be very accurate in calculations of ratios of elastic backscattering probabilities for different pairs of elemental solids and in different experimental configurations [10]. This shows that a crucial problem to solve is the determination of the angular distribution of electron directions after k collisions, $H_k(\theta)$. In computational practice, main problem to solve is the determination of the series of parameters, A_l, l = 0, 1, 2, ... Calculations at this stage may need a considerable amount of the computer time, and thus it can hinder the use of Eq. (1) in practical EPES analysis. This problem is addressed in the next section.

2.2. Parameters A_l

In principle, the parameters A_l can be calculated from Eq. (3) if the elastic scattering cross section is known with high accuracy and for a dense grid of scattering angles, θ. However this approach may lead to large systematic errors for large values of index l since the Legendre polynomial becomes then a highly oscillating function. A recommended approach is based on the relation of the parameters A_l to the phase shifts [10]. A given relativistic elastic-scattering cross section can be expressed by a series of "spin-up" and "spin-down" phase shifts designated by δ_n^+ and δ_n^-, respectively,

$$\frac{d\sigma_{el}}{d\Omega} = |f(\theta)|^2 + |g(\theta)|^2 \tag{8}$$

where

$$f(\theta) = \frac{1}{2iK}\sum_{n=0}^{\infty}\{(n+1)[\exp(2i\delta_n^+)-1] + n[\exp(2i\delta_n^-)-1]\}P_n(\cos\theta), \tag{9}$$

$$g(\theta) = \frac{1}{2iK}\sum_{n=0}^{\infty}[\exp(2i\delta_n^-) - \exp(2i\delta_n^+)]P_n^1(\cos\theta), \tag{10}$$

n = 0, 1, … is the angular momentum quantum number, K is the wave number of an electron, and $P_n^1(\cos\theta)$ are the associated Legendre functions. From Eqs (3), (8)-(10), an analytical relation between the parameters A_l and the phase shifts can be derived [8,10]. The relevant formalism is summarized in Appendix 1.

It has been shown that the elastic scattering cross sections calculated for the Dirac-Hartree-Fock (DHF) potential better compare with the experimental data than the cross sections corresponding to the Thomas-Fermi-Dirac potential (TFD) [19]; both potentials are frequently used to describe an interaction between an electron and atoms constituting a given solid. However, the DHF potential needs a considerably larger number of phase shifts for the elastic scattering cross section than the TFD potential. Suppose that the angular momentum quantum number, n, needed for a given element and energy varies in the range $0 \le n \le n_{\max}$. For 10 keV electrons scattered on gold, $n_{\max} = 325$ for the DHF potential while $n_{\max} = 141$ for the TFD potential [19]. Despite of this problem, it is advisable to base calculations of the A_l parameters on the DHF potential since we may expect that the results obtained are more realistic as compared to results from the TFD potential. Furthermore, the phase shifts for the DHF potential for all elements and a wide range of energies are relatively easily available. The phase shifts δ_n^+ and δ_n^- can be calculated from the software ELSEPA [20]. The relevant computer code is available from Computer Physics Communications Program Library [21]. These phase shifts can also be obtained from the NIST database [22]. The absolute values of phase shifts obtained from these sources at $n_{\max}$ decrease down to values smaller that 10^{-8} (ref. [22]) or 10^{-9} (refs [20,21]). As shown in Fig. 3(a), the number of phase shifts, $n_{\max}$, increases with electron energy. The largest number is observed for cesium at 5000 eV ($n_{\max} = 460$). At a given energy, the $n_{\max}$ value depends considerably on element as illustrated in Fig. 3(b).

The series of phase shifts calculated from the software ELSEPA for a given energy and element ensures accuracy of the scattering amplitudes [Eqs. (9) and (10)] within at least six significant digits [20].

The series defining the angular distribution $H_k(\theta)$ [Eq. (2)] also turns out to be relatively slowly convergent. Let us denote by $l_{\max}$ the needed number of parameters A_l to describe the distribution of scattering angles after one collision

$$H_1(\theta) = \frac{1}{\sigma_{el}} \frac{d\sigma_{el}}{d\Omega} = \frac{1}{2\pi} \sum_{l=0}^{\infty} \frac{2l+1}{2} A_l \; P_l(\cos\theta) \tag{11}$$

The number $l_{\max}$ may exceed the number of phase shifts, $n_{\max}$, when the accuracy of $H_1(\theta)$ better than 6 decimals is required. For this reason, Eq. (3) is not suitable to use in calculations of parameters A_l due to problems of numerical integration. The formalism summarized in Appendix 1 [Eq. (B6)] is recommended for that purpose. Despite of an apparent complexity, the relevant algorithm is very stable. The only major computational difficulty is the determination of the Wigner 3j symbol values, $\begin{pmatrix} l & n & k \\ 0 & 0 & 0 \end{pmatrix}$ and $\begin{pmatrix} l & n & k \\ 0 & 1 & -1 \end{pmatrix}$, for large values of parameters *l*, *n* and *k*. One can use the integral representations of both Wigner 3j symbols

$$\begin{pmatrix} l & n & k \\ 0 & 0 & 0 \end{pmatrix} = \left(\frac{1}{2} \int_0^{\pi} P_l(\cos\theta) \; P_n(\cos\theta) \; P_k(\cos\theta) \sin\theta \; d\theta \right)^{1/2} \tag{12}$$

(13)

$$\begin{pmatrix} l & n & k \\ 0 & 1 & -1 \end{pmatrix} \begin{pmatrix} l & n & k \\ 0 & 0 & 0 \end{pmatrix} = -\frac{1}{2\left[n(n+1)k(k+1)\right]^{1/2}} \int_0^{\pi} P_l(\cos\theta) P_n^1(\cos\theta) P_k^1(\cos\theta) \sin\theta \; d\theta$$

However, the integrands become highly oscillating functions for large parameters *l*, *n* and *k* which leads to difficulties in convergence of a quadrature used. An alternative analytical algorithm suitable for this purpose has recently been tested and recommended [10].

In the present work, Eq. (B6) has been used in calculations of A_l parameters for all elements and for 200 energies from 50 eV to 5000 eV uniformly distributed in the logarithmic scale. As follows from Eq. (3), the parameter A_0 is always equal to unity. The maximum value of the index l considered here for a given element and energy was equal to doubled maximum value of the phase shifts, $2n_{\max}$. As an example, first 50 parameters A_l calculated for gold are shown in Fig. 4 as a 3D plot. We see that, in double logarithmic coordinates, the parameters A_l is a smooth function of energy. Only in the region $1 \le l \le 10$ some structure is observed. Details of this region are visualized in Fig. 5. We may state that the parameters A_l for any energy can be obtained by interpolation of the energy dependence of A_l in doubly logarithmic coordinates. Thus, the database of parameters A_l calculated here is a convenient basis for calculating the angular distributions, $H_k(\theta)$, and consequently, in calculations of the probability of elastic backscattering, $d\eta / d\Omega$.

2.3. Alloys and compounds

As mentioned in the Introduction, practical application of the analytical formalism requires an extension to samples constituted of different atomic species. Below, a relevant modification of the formalism is proposed.

Let us consider an electron which is elastically scattered by two different atomic species, as outlined in Fig. 6. The first scattering event is described by the polar scattering angle, θ_1, and the azimuthal scattering angle, φ_1. Similarly, the second collision is characterized by the angles θ_2 and φ_2. The angle θ measured with respect to the initial direction is then given by

$$\cos\theta = \cos\theta_1 \cos\theta_2 + \sin\theta_1 \sin\theta_2 \cos(\varphi_1 - \varphi_2) \qquad (14)$$

According to the addition theorem of the Legendre polynomials, we have then [23]

$$P_l(\cos\theta) = P_l(\cos\theta_1)P_l(\cos\theta_2) + 2\sum_{m=0}^{l}\frac{(l-m)!}{(l+m)!}P_l^m(\cos\theta_1)P_l^m\cos(\theta_2)\cos m(\varphi_1-\varphi_2) \qquad (15)$$

Suppose that the angles θ_1, φ_1, θ_2 and φ_2 are described by independent probability density functions. If the angles φ_1, and φ_2 are uniformly distributed, one can prove that the second term in Eq. (15) vanishes [24]. We eventually obtain the following relation between mean values of Legendre polynomials $P_l(\cos\theta)$, $P_l(\cos\theta_1)$ and $P_l(\cos\theta_2)$

$$< P_l(\cos\theta) > = < P_l(\cos\theta_1) > < P_l(\cos\theta_2) > \qquad (16)$$

If the angles θ, θ_1, θ_2 occur with probabilities described by the probability density functions $f(\theta)$, $f^{(A)}(\theta_1)$ and $f^{(B)}(\theta_2)$, Eq. (16) can be rewritten in the form

(17)

$$\int_0^{\pi} f(\theta)P_l(\cos\theta)\sin\theta\, d\theta = \int_0^{\pi} f^{(A)}(\theta_1)P_l(\cos\theta_1)\sin\theta_1\, d\theta_1 \times \int_0^{\pi} f^{(B)}(\theta_2)P_l(\cos\theta_2)\sin\theta_2\, d\theta_2$$

After substitution $x = \cos\theta$, we obtain

$$\int_{-1}^{1} f(x)P_l(x)\,dx = \int_{-1}^{1} f^{(A)}(x)P_l(x)\,dx \times \int_{-1}^{1} f^{(B)}(x)P_l(x)\,dx \qquad (18)$$

Since the functions $\left(\frac{2l+1}{2}\right)^{1/2} P_l(x)$ form a set of normalized orthogonal polynomials, we may write

$$f(x) = \sum_{l=0}^{\infty}\left(\frac{2l+1}{2}\right) g_l\, P_l(x) \qquad (19)$$

where

$$g_l = \int_{-1}^{1} f(x)P_l(x)dx \qquad (20)$$

Eqs (18)-(20) can be transformed as follows

$$f(x)=\sum_{l=0}^{\infty}\left(\frac{2l+1}{2}\right)P_l(x)\int_{-1}^{1}f(x)P_l(x)dx= \tag{21}$$

$$\sum_{l=0}^{\infty}\left(\frac{2l+1}{2}\right)P_l(x)\left[\int_{-1}^{1}f^{(A)}(x)P_l(x)dx\times\int_{-1}^{1}f^{(B)}(x)P_l(x)dx\right]=$$

$$\sum_{l=0}^{\infty}\left(\frac{2l+1}{2}\right)g_l^{(A)}g_l^{(B)}P_l(x)$$

where

$$g_l^{(A)}=\int_{-1}^{1}f^{(A)}(x)\,P_l(x)dx \tag{22a}$$

$$g_l^{(B)}=\int_{-1}^{1}f^{(B)}(x)\,P_l(x)dx \tag{22b}$$

Suppose that a binary compound consists of two atomic species A and B with a certain stoichiometry defined by the atom fractions x_A and x_B, respectively. We assume that the probabilities of elastic scattering events on atoms A and B is equal to p_A and p_B. Four cases are then possible:

Order of collisions	Probability
A – A	p_A^2
A – B	$p_A p_B$
B – A	$p_B p_A$
B – B	p_B^2

Eq. (21) can be then written for a binary compound as follows

$$f^{comp}(x)=\sum_{l=0}^{\infty}\left(\frac{2l+1}{2}\right)P_l(x)\left[p_A^2(g_l^{(A)})^2+2p_Ap_Bg_l^{(A)}g_l^{(B)}+p_B^2(g_l^{(B)})^2\right]= \tag{23}$$

$$\sum_{l=0}^{\infty}\left(\frac{2l+1}{2}\right)P_l(x)\left(p_Ag_l^{(A)}+p_Bg_l^{(B)}\right)^2$$

Let us generalize this expression for the case of n collisions. Suppose that n_A scattering events occurred on atoms A and n_B on atoms B. Such events can be arranged in $\frac{n!}{n_A!n_B!}$ ways which is given by the number of combinations. Thus

$$f^{comp}(x) = \sum_{l=0}^{\infty}\left(\frac{2l+1}{2}\right)P_l(x)\sum_{n_A=0}^{n}\frac{n!}{n_A(n-n_A)}p_A^{n_A}(g_l^{(A)})^{n_A}\,p_B^{n-n_A}(g_l^{(B)})^{n-n_A} \tag{24}$$

Finally

$$f^{comp}(x) = \sum_{l=0}^{\infty}\left(\frac{2l+1}{2}\right)g_l^{comp}P_l(x) \tag{25}$$

where $g_l^{comp} = \left(p_A g_l^{(A)} + p_B g_l^{(B)}\right)^n$

The generalization to a compound consisting of m atomic species is then straightforward

$$g_l^{comp} = \left(\sum_{i=1}^{m} p_i g_l^{(i)}\right)^n \tag{26}$$

We assume now that the angular distribution of scattering angles after single scattering event on i-th atomic species is $f^{(i)}(x) \equiv H_1^{(i)}(x)$. In that case, obvious identities follow

$$g_l^{(i)} \equiv A_l^{(i)} \tag{27a}$$

$$A_l^{comp} = \left(\sum_{i=1}^{m} p_i A_l^{(i)}\right)^n \tag{27b}$$

The probability that the elastic scattering event occurs on i-th atomic species can be calculated from expression typically used in Monte Carlo simulations of electron transport in compounds or alloys [25,26]

$$p_i = \frac{x_i\sigma_{el,i}}{\sum_{j=1}^{m} x_j\sigma_{el,j}} \tag{28}$$

where x_i is the atom fraction of *i*-th component. Thus, the elastic backscattering probability for a given compound cal be calculated from Eqs (1) and (2) after introducing in Eq. (2) the parameter A_l^{comp} determined from Eqs (27b) and (28).

For completeness, we also need the transport parameter, *s*, determined for a compound from Eq. (5). The IMFP for a compound, λ_{in}, can be estimated from the predictive formula TPP-2M [27]. These data are also available from the NIST database [28]. One can calculate the elastic mean free path, λ_{el}, from Eq. (6) in which the atomic density and the total elastic scattering cross section are evaluated for a compound. The atomic density, N^{comp}, is described by the expression typically used in the formalism of electron probe microanalysis [18]

$$N^{comp} = N_A \rho \sum_{i=1}^{m} \frac{c_i}{M_i} = N_A \rho \left(\sum_{i=1}^{m} x_i M_i \right)^{-1} \tag{29}$$

where ρ is the density of a compound, c_i is the atom fraction of *i*-th element, and M_i is the corresponding atomic mass. The total elastic cross section for a compound is expressed by

$$\sigma_{el}^{comp} = \sum_{i=1}^{m} x_i \sigma_{el,i} \tag{30}$$

Eventually

$$\lambda_{el}^{comp} = \frac{1}{N_A \rho} \frac{\sum_{i=1}^{m} x_i M_i}{\sum_{i=1}^{m} x_i \sigma_{el,i}} \quad , \tag{31}$$

2.4. Monte Carlo simulation strategy

The elastic electron backscattering probabilities were also calculated here from algorithms based on Monte Carlo simulations. Details of the simulation strategy for elements

have been described in details in a recent paper [10]. For compounds, a similar modification of strategy was made here as in the Monte Carlo simulations of Auger electron [25] or photoelectron [26] transport. The length of linear step between elastic collisions, Λ, was assumed to be described by the exponential distribution

$$F(\Lambda) = \frac{1}{\lambda_{el}^{comp}} \exp\left(-\frac{\Lambda}{\lambda_{el}^{comp}}\right) \tag{32}$$

where the elastic mean free path, λ_{el}^{comp}, is calculated from Eq. (31). After passing the generated step length, the kind of an atom is selected according to probabilities given by Eq. (28). The polar scattering angle after the elastic collision is generated from the probability density function, $H_1^{(i)}(\theta)$, where index *i* designates the selected atomic species

$$H_1^{(i)}(\theta) = \frac{1}{\sigma_{el}^{(i)}} \frac{d\sigma_{el}^{(i)}}{d\Omega} \tag{33}$$

Calculations of the elastic backscattering probability, $\Delta\eta$, are performed for a finite size of an analyzer solid acceptance angle, $\Delta\Omega$ (see Fig. 1). The solid angle should not be too small to get a reasonably accurate statistics of electrons entering the analyzer after an acceptable amount of computations. In practice, assumption of the half-cone angle, $\Delta\alpha$, equal to $4° \div 5°$ is manageable. In that case, the number of generated trajectories should be of the order of 10^7 to estimate the probability $\Delta\eta$ with accuracy of 1% - 2%.

3. Results

3.1. Angular distribution of elastically backscattered intensity

Much experimental material on angular distribution of the elastically backscattered current is available in the literature [5,11,29-35]. Majority of published data originates from experiments in which a movable analyzer with a small acceptance angle was used.

Information on the angular distribution can also be obtained from processing of images of elastically backscattered electrons using the LEED optics [30,32]. In the present work, the angular distributions measured for 10 elements (Si, Fe, Co,Ni, Cu, Pd, Ag, Sm, Ir and Au) have been selected as a reference for evaluation of theoretical models described here [33,34]. These data were obtained by measurements of the elastic peak intensity using an angle resolved photoelectron spectrometer (ADES 400, VG Scientific, UK) equipped with a rotatable hemispherical analyzer. The half-cone angle of the analyzer was equal to $\pm 4.1°$. Electron beam was situated at normal to the sample surface, while the analyzer was moved in the range $35° \le \alpha \le 74°$. The angular distribution was described by the elastic peak intensities, $I^{(\exp)}$, as a function of the emission angle, α.

Eq. (1) describes the elastically backscattered probability within an infinitely small acceptance angle. Let us assume that the distribution $d\eta/d\Omega$ is practically constant within a small acceptance angle of an analyzer used in measurements. We may write then

$$\Delta\eta^{(AN)} = \int_{\Delta\Omega} \frac{d\eta}{d\Omega} d\Omega = 2\pi \int_0^{\Delta\alpha} \frac{d\eta}{d\Omega} \sin\alpha \, d\alpha \cong 2\pi(1-\cos\Delta\alpha)\frac{d\eta}{d\Omega} \tag{34}$$

where the index *AN* indicates the analytical theory. The Monte Carlo simulations performed for the actual solid angle of an analyzer provide the elastic backscattering probabilities, $\Delta\eta^{(MC)}$. In the present calculations, the IMFPs for all elements with exception of samarium were taken from Tanuma et al. [36]. For samarium, the predictive formula TPP-2M [27] was used. The calculated dependences of elastic backscattering probabilities, $\Delta\eta^{(AN)}$ or $\Delta\eta^{(MC)}$, were fitted at a given energy to the experimental intensities by choosing parameter *C* such that the squared differences $[C\Delta\eta - I^{(\exp)}]^2$ were minimized. The resulting comparisons of experimental data and predictions of the theoretical models considered here are shown in Figs 7-10 for Ni, Cu, Ag and Au, i.e. for reference materials recommended for measurements of

the IMFP [35,37]. Two conclusions result from these comparisons. Generally, the theoretical models describe very well the shape of the measured dependence of backscattered intensities, $I^{(\exp)}$, on the emission angle, α. Second, the AN and the MC theoretical models, after fit to experimental data, describe the shape of the measured angular dependence with comparable quality. Furthermore, the agreement between theory and experiment seems to improve with increasing energy.

To quantify the comparison of the experimental data and the theoretical models used in calculations, the mean percentage differences were calculated. For comparison of the measured intensities, $I^{(\exp)}$, and the calculated probabilities of elastic backscattering after fit, $C\Delta\eta^{(AN)}$, the following criterion for a given element and energy was used

$$R_{AN} = \frac{1}{m}\sum_{k=1}^{m}\left|\Delta_k^{(AN)}\right| \tag{35}$$

where

$$\Delta_k^{(AN)} = 100\frac{C\,\Delta\eta_k^{(AN)} - I_k^{(\exp)}}{C\,\Delta\eta_k^{(AN)}} \tag{36}$$

and m is the number of measured intensities at a given energy. The mean percentage differences, R_{AN}, are listed in Table 1. For each element, these values are further averaged with respect to all three energies according to the rule

$$< R_{AN} >= 100\frac{1}{m_1+m_2+m_3}\sum_{i=1}^{3}\sum_{k=1}^{m_i}\left|\frac{C_i\Delta\eta_{i,k}^{(AN)} - I_{i,k}^{(\exp)}}{C_i\Delta\eta_{i,k}^{(AN)}}\right|, \tag{37}$$

where m_1, m_2 and m_3 are the numbers of measurements at three energies. The averaged mean percentage differences $< R_{AN} >$ are listed in Table 1 and in Figs 7-10.

Similar criteria were used to quantify the difference between the measured intensities, $I^{(\exp)}$, and the fitted probabilities of elastic backscattering resulting from Monte Carlo

simulations, $C\Delta\eta^{(MC)}$. The mean percentage differences, R_{MC}, and the averaged mean percentage differences, $< R_{MC} >$, are listed in Table 2. The R_{MC} values are practically identical with published data [33] which were estimated from a slightly different Monte Carlo program (another source of IMFPs and a different sampler of elastic scattering angles). The averaged mean percentage differences, $< R_{MC} >$, were also published for a Monte Carlo code [34]. Again, they are very close to the values listed in Table 2 and in Figs 7-10. They vary between 3.75% and 12.73% with the total average of 6.64.

On comparison of deviations listed in Tables 1 and 2, we see that the percentage differences R_{AN} and $< R_{AN} >$ are only slightly larger than the differences R_{MC} and $< R_{MC} >$. The averaged mean percentage differences, $< R_{AN} >$, vary between 6.54% and 14.10% with total average of 8.84%. Assumptions made in the analytical model that simplify the description of the electron transport (domination of one large-angle collision) and in the computational algorithm (interpolation of the A_l parameters) have only an insignificant influence on the calculated elastic backscattering intensity as compared to the Monte Carlo algorithm.

3.2. Ratios of elastic peak intensities

An important application of EPES is the experimental determination of the IMFP for a given solid. Considerable volume of IMFPs resulting from this method is available in the literature [28,37-40]. A recommended experimental procedure involves measurements of ratios of the elastic peak intensities for a studied sample and for the reference material [37]. This procedure must be accompanied with a reliable theory that provides these ratios with possibly high accuracy. In a considerable majority of the published material, the Monte Carlo simulations are used in relevant calculations.

Tanuma et al. [40] reported the energy dependence of ratios of elastic peak intensities in a wide energy range from 50 eV to 5000 eV. Measurements were performed for 13 elemental solids [C (graphite), Si, Cr, Fe, Cu, Zn, Ga, Mo, Ag, Ta, W, Pt and Au]. According to earlier recommendation [37], the nickel sample was used as a reference material. A unique construction of the cylindrical mirror analyzer (CMA) was used in these studies with a typical solid acceptance angle ($\alpha = 42.3° \pm 6°$) [41]. This analyzer, after careful calibration, made possible determination of the absolute signal intensities in the geometry of measurements, $I^{(\mathrm{exp})}$ and $I_{Ni}^{(\mathrm{exp})}$, for a given sample and the reference sample, respectively. Consequently, one can consider the reported ratios,

$$\Gamma^{(T)} = I^{(\mathrm{exp})} / I_{Ni}^{(\mathrm{exp})}, \tag{38}$$

as the most accurate database of experimental ratios appropriate for evaluation of theoretical models considered here.

The MC and AN theoretical models were used in calculations of all reported experimental ratios. Similarly as in the previous section, the IMFPs were taken from Tanuma et al. [36] with exception of gallium. For the latter element, the IMFPs were evaluated from the TPP-2M predictive formula [37]. Let us introduce the following notation for the calculated ratios

$$\Gamma^{(MC)} = \Delta\eta^{(MC)} / \Delta\eta_{Ni}^{(MC)} \tag{39a}$$

$$\Gamma^{(AN)} = \Delta\eta^{(AN)} / \Delta\eta_{Ni}^{(AN)} \tag{39b}$$

where the superscript denotes the theoretical model used. The experimental ratios, $I^{(\mathrm{exp})} / I_{Ni}^{(\mathrm{exp})}$, are compared with results of calculations in Figs 11-13. We note that the energy dependences of calculated ratios, $\Gamma^{(MC)}$ and $\Gamma^{(AN)}$ are practically identical with exception of graphite and silicon for energies below 200 eV. As a consequence, the ratios calculated from both theoretical models describe the experimentally determined dependence with a similar

accuracy. The differences between experimental and theoretical ratios can be ascribed partly to limitations of theoretical models, especially in the region of low energies, and partly to inaccuracies in the IMFPs used in calculations. We may expect that the IMFPs calculated from the optical data [27,36] may differ from the IMFPs that are valid for the surface region of the studied samples.

The deviations between experimental ratios and theoretical ratios shown in Figs 11-13 were described by the following percentage differences

$$\Delta\Gamma^{T-AN} = 100\,\frac{\Gamma^{(T)} - \Gamma^{(AN)}}{\Gamma^{(T)}} \tag{40a}$$

$$\Delta\Gamma^{T-MC} = 100\,\frac{\Gamma^{(T)} - \Gamma^{(MC)}}{\Gamma^{(T)}} \tag{40b}$$

while the deviations due to two theoretical models were defined by

$$\Delta\Gamma^{MC-AN} = 100\,\frac{\Gamma^{(MC)} - \Gamma^{(AN)}}{\Gamma^{(MC)}} \tag{40c}$$

These percentage differences are plotted in Figs 14-16. We see that the percentage deviations between theory and experiment, $\Delta\Gamma^{T-AN}$ and $\Delta\Gamma^{T-MC}$, for energies below 200 eV may reach or even exceed 80% (e.g., C, Ag, W, Pt and Au). Better agreement, typically less than 20%, is observed for higher energies. In contrast, the percentage differences between the theoretical models, $\Delta\Gamma^{MC-AN}$, are much smaller and generally they do not exceed 20%, with exception of graphite and silicon.

The percentage differences, $\Delta\Gamma^{T-AN}$, $\Delta\Gamma^{T-MC}$ and $\Delta\Gamma^{MC-AN}$, were averaged over all energies considered

$$<\Delta\Gamma> = \frac{1}{m}\sum_{i=1}^{m}\left|\Delta\Gamma\right| \tag{41}$$

where *m* is the number of ratios measured for a given sample. The resulting mean percentage differences, $<\Delta\Gamma^{T-AN}>$, $<\Delta\Gamma^{T-MC}>$ and $<\Delta\Gamma^{MC-AN}>$, are listed in Table 3. Good

agreement between both theoretical models is observed. The mean deviations $<\Delta\Gamma^{MC-AN}>$ range between 0.67% and 9.26% with the total mean of 4.46%. The mean deviations $<\Delta\Gamma^{T-AN}>$ and $<\Delta\Gamma^{T-MC}>$ are much larger, with total mean of about 16%. These deviations can be reduced by proper choice of IMFPs in calculations of ratios $\Gamma^{(MC)}$ and $\Gamma^{(AN)}$.

3.3. Inelastic mean free paths for elemental solids

Application of EPES to determine the IMFP consists in selecting a value of the IMFP for a given sample in such a way that the calculated ratio of the elastic backscattering probabilities is equal to the measured ratio of elastic peak intensities. In other words, we need to solve the following equation with respect to λ_{in}

$$\Delta\eta(\lambda_{in})/\Delta\eta_{Ni} = I^{(\exp)}/I_{Ni}^{(\exp)} \tag{42}$$

Tanuma et al. [40] determined the IMFPs for 13 elemental solids from the ratios reported by these authors. The ratios $\Delta\eta/\Delta\eta_{Ni}$ were calculated from Monte Carlo simulations. The IMFPs for 13 elements were also determined in the present work from the same experimental ratios, $I^{(\exp)}/I_{Ni}^{(\exp)}$. To solve Eq. (42), the analytical theoretical model and the Monte Carlo strategy described here were used. Results presently obtained are compared with IMFPs of Tanuma et al. [40] in Figs 17-19. For completeness, the IMFPs calculated from the optical data [36] and data obtained using the TPP-2M predictive formula [27] are also shown there. In practically all cases, the IMFPs obtained from the analytical model, $\lambda_{in}^{(AN)}$, and the Monte Carlo algorithm described here, $\lambda_{in}^{(MC)}$, are very similar. The noticeable differences are observed only for graphite and silicon at energies below about 200 eV. The IMFPs determined by Tanuma et al. [40], $\lambda_{in}^{(T)}$, agree well with values $\lambda_{in}^{(AN)}$ and $\lambda_{in}^{(MC)}$ at energies

exceeding 200 eV. In the range of lower energies, for some elements (e.g. C, Si and Mo), the deviation of $\lambda_{in}^{(T)}$ from $\lambda_{in}^{(AN)}$ and $\lambda_{in}^{(MC)}$ is much more pronounced than the difference between $\lambda_{in}^{(AN)}$ and $\lambda_{in}^{(MC)}$.

To quantify the observed deviations, the following percentage differences were calculated

$$\Delta\lambda_{in}^{T-AN} = 100\,\frac{\lambda_{in}^{(T)} - \lambda_{in}^{(AN)}}{\lambda_{in}^{(T)}} \tag{43a}$$

$$\Delta\lambda_{in}^{T-MC} = 100\,\frac{\lambda_{in}^{(T)} - \lambda_{in}^{(MC)}}{\lambda_{in}^{(T)}} \tag{43b}$$

$$\Delta\lambda_{in}^{MC-AN} = 100\,\frac{\lambda_{in}^{(MC)} - \lambda_{in}^{(AN)}}{\lambda_{in}^{(MC)}} \tag{43c}$$

They are shown in Figs 20-22. The largest differences between IMFPs published by Tanuma et al. [40], $\lambda_{in}^{(T)}$, and determined in the present work, $\lambda_{in}^{(AN)}$ and $\lambda_{in}^{(MC)}$, for C, Si and Mo reach or even exceed 60%. For energies exceeding 200 eV, these percentage deviations are much smaller and typically do not exceed 20%. The differences between IMFPs calculated in the present work, $\lambda_{in}^{(AN)}$ and $\lambda_{in}^{(MC)}$, are rather small; in practically all cases they are smaller than 10%. Thus, the uncertainties due to differences in the Monte Carlo code of Tanuma et al. [40] and the code used in the present work may be larger than the deviation due to differences betwee the theoretical models considered here. To approach closer this issue, the percentage differences given by Eqs (43a)-(43c) were averaged over a given energy range according to the general formula

$$< \Delta\lambda_{in} >= \frac{1}{m}\sum_{i=1}^{m} \left|\Delta\lambda_{in}\right| \tag{44}$$

Two energy ranges were considered: (i) the total energy range from 50 eV to 5000 eV' and (ii) the energy range in which the IMFPs are in a good agreement, i.e. the range from 200 eV

to 5000 eV. Results are listed in Table 4. We note that the mean percentage difference due to the theoretical models considered here is rather small. The total average is equal to 4.24%. This value weakly depends on the energy range. For the range from 200 eV to 5000 eV, the total average decreases by slightly more than one percent, i.e. down to 3.09%. The averaged difference between results of Monte Carlo calculations of Tanuma et al. [40] and present Monte Carlo results is larger, i.e. 9.42% for the total energy range, and it distinctly decreases down to 5.73% for energies exceeding 200 eV.

3.4. Inelastic mean free paths for alloys and compounds

Let us check the validity of proposed extension of the analytical formalism to compounds and alloys. We consider here the procedure of determination of the IMFP for such solids from the measured ratios of elastic peak intensities for a studied sample and a given reference material. This analysis is performed for five arbitrarily selected solids: the $Al_{0.48}Ni_{0.52}$ alloy [42], gallium antimonide [43]; indium antimonide [43]; gallium nitride [44] and silicon carbide [45]. Summary of an algorithm implementing the extended analytical formalism is the following. The elastic backscattering probability is calculated from Eqs (1) and (2) with parameters A_l replaced with A_l^{comp}. The latter parameters are calculated from Eqs (27b) and (28). The elastic mean free path, λ_{el}, needed for the parameter *s* defined by Eq. (5), is calculated from Eq. (6). The atomic density, *N*, and the total elastic scattering cross section, σ_{el}, are replaced with parameters N^{comp} and σ_{el}^{comp} given by Eqs (29) and (30), respectively. The IMFP, λ_{in}, needed for parameter *s* can be calculated from the predictive formula TPP-2M [27] or adjusted so that an agreement with the measured ratio of elastic peaks is reached. Thus, we see that the input parameters for calculations are: (i) atomic numbers and atomic masses of all species constituting a given compound; (ii) stoichiometry

coefficients (or atomic fractions); (iii) density of a compound. The same input parameters are needed for the Monte Carlo algorithm simulating electron transport in a compound. The only difference is in the input parameters describing the elastic scattering events; instead of parameters $A_l^{(i)}$ we need the differential elastic scattering cross sections $d\sigma_{el}^{(i)}/d\Omega$ [see Eq. (33)].

Comparison of the IMFPs resulting from the analytical formalism, $\lambda_{in}^{(AN)}$, and from the Monte Carlo calculations, $\lambda_{in}^{(MC)}$, with the published IMFPs, $\lambda_{in}^{(MC)}$, is shown in Figs 23(a)-23(e). We see that all three IMFPs well agree in all cases. An important conclusion resulting from these results is a high accuracy of the extended analytical formalism, practically reproducing IMFPs from the Monte Carlo calculations. The IMFPs calculated here agree well with the published data. In cases when the Monte Carlo calculations were used for processing of the measured ratios [43-45], this result is expected. However, the IMFPs for $Al_{0.48}Ni_{0.52}$ were derived from an oversimplified theory of electron backscattering in which the multiple elastic scattering events are neglected (single large-angle backscattering model – SLAB); accuracy of this model has recently been extensively analyzed [10]. Furthermore, the elastic scattering cross sections were calculated from the nonrelativistic theory assuming the TFD potential. Thus, the observed agreement between the IMFPs calculated here and the published IMFPs seems to be fortuitous. Finally, one should also indicate a reasonable agreement of all IMFPs with the IMFPs obtained from the predictive formula.

Let us calculate for the considered compounds, using Eq. (43c), the percentage deviations, $\Delta\lambda_{in}^{MC-AN}$, between IMFPs calculated from the analytical formalism and from Monte Carlo simulations. They are shown in Figs 24(a) -24(e). In practically all cases, the percentage differences do not exceed 5%. The only distinct exception is the IMFP for InSb at 500 eV where the deviation reaches 10%. [Fig. 24(c)]. For comparison, the percentage

deviations between published IMFPs, $\lambda_{in}^{(PUBL)}$, and the IMFPs calculated from algorithms developed here, $\lambda_{in}^{(AN)}$ and $\lambda_{in}^{(MC)}$,

$$\Delta\lambda_{in}^{PUBL-AN} = 100\,\frac{\lambda_{in}^{(PUBL)} - \lambda_{in}^{(AN)}}{\lambda_{in}^{(PUBL)}} \tag{45a}$$

$$\Delta\lambda_{in}^{PUBL-MC} = 100\,\frac{\lambda_{in}^{(PUBL)} - \lambda_{in}^{(MC)}}{\lambda_{in}^{(PUBL)}} \tag{45b}$$

are also plotted in Figs 24(a) -24(e). These deviations are generally larger than the deviations $\Delta\lambda_{in}^{MC-AN}$ exceeding even 20% [see Fig. 24(c)]. This is an another proof that the use of the two Monte Carlo codes may lead to uncertainties in the IMFPs which are larger than the percentage differences between the analytical formalism and the Monte Carlo code used here. This issue is approached in detail in the next section.

4. Discussion

Recently, it has been indicated that the elastic backscattering probabilities calculated from the analytical formalism are underestimated as compared to the values obtained from Monte Carlo simulations [10]. This underestimation evaluated for the emission angles $0° \le \alpha \le 74°$ and for energies 200 eV $\le E \le$ 5000 eV was equal to 8.08% (or 8.87% for the energy range 200 eV $\le E \le$ 1000 eV). In the present work, we have compared the shape of the energy dependence of measured elastically backscattered intensity with calculated energy dependences (see Figs 7-10). For this comparison, the calculated data were fitted to experimental intensities. As follows for Tables 1 and 2, both theoretical models considered here describe the shape of experimental energy dependence with similar accuracy: the averaged mean percentage deviation $< R_{MC} >$ is equal to 6.64% while $< R_{AN} >$ is equal to

8.84%. Thus, the difference is only 2.2%. If the shape of energy dependences is similar, the underestimation of the elastically backscattered intensity is largely removed if we consider ratio of intensities rather than the absolute intensities.

Similar conclusion resulted from comparison of ratios of elastic backscattering probabilities calculated from the analytical model with ratios from Monte Carlo simulations [10]. The difference between ratios of different combinations of elements averaged over an energy range 200 eV – 5000 eV was equal to only 3.14% [10]. For this reason, the analytical formalism is a very prospective tool for determination of the IMFPs. We note, however, that the deviation between ratios measured by Tanuma et al. [40] and the ratios calculated here is rather significant. As follows from Table 3, the mean percentage deviations, $<\Gamma^{T-AN}>$ and $<\Gamma^{T-MC}>$, are equal to 15.99% and 16.04%, respectively. This effect is due to the fact that the IMFPs used in calculations (from refs [27] and [36]) may differ from the IMFPs valid for the surface region of studied solids. We may expect that proper adjustment of the IMFPs would decrease these percentage deviations. Nonetheless, the averaged mean percentage differences between ratios calculated from theoretical models used here are rather small; the averaged mean percentage difference $<\Gamma^{MC-AN}>$ is equal to 4.46%. This result is another support for accuracy and reliability of the analytical formalism. Although this value is slightly larger than the mean percentage difference equal to 3.14% reported in ref [10], one should note that the present averaging was extended over larger energy range, i.e. from 50 eV to 5000 eV.

The IMFPs determined here from two theoretical models using intensity ratios published by Tanuma et al. [40] agree very well. As follows from Table 4, the averaged mean percentage deviation, $<\Delta\lambda_{in}^{MC-AN}>$, is equal 4.24%. However, the mean deviations of the presently determined IMFPs from the IMFPs published by Tanuma et al. [40], $<\Delta\lambda_{in}^{T-AN}>$

and $<\Delta\lambda_{in}^{T-MC}>$, are more than twice larger. As shown in Figs 14-16, the largest scatter is generally observed in the energy range from 50 eV to 200 eV. In particular, the deviations $\Delta\lambda_{in}^{T-MC}$ are due to differences in the Monte Carlo program designed here and the code used by Tanuma et al. [40]. Let us discuss briefly the origin of these differences.

Tanuma et al. [40] identified possible source of deviations as due the use of the TFD potential in calculations of elastic scattering cross sections. These authors found that the difference between calculated ratios of intensities resulting from the use of TFD and DHF potentials vary between 14% and 20% for Si and Ag at 100 eV and 200 eV. For energies exceeding 1000 eV, the differences were typically 5%. These results are confirmed in the present work. As shown in Figs 20-22, the largest values of percentage differences $\Delta\lambda_{in}^{T-MC}$ are observed indeed below 200 eV. For graphite, silicon, and molybdenum, the differences reach or even exceed 60%. Fig. 25 shows the differential elastic scattering cross sections at 50 eV for these elements. Noticeable differences between the elastic scattering cross sections are visible. Lower panels show the percentage deviations calculated from

$$\Delta DCS = 100\frac{(d\sigma_{el}/d\Omega)_{DHF} - (d\sigma_{el}/d\Omega)_{TFD}}{(d\sigma_{el}/d\Omega)_{DHF}} \quad (46)$$

These percentage deviations are significant at 50 eV; they reach 47% for carbon, 69 for silicon and 160% for molybdenum. In fact, the difference between cross sections was extensively analyzed by Jablonski et al. [19] on example of noble gases since for these elements the experimental data for energies from 50 eV to 3000 eV are available. It has been shown that the difference between cross sections is the most pronounced at low energies and decreases with energy. The experimental cross sections seem to agree better with $(d\sigma_{el}/d\Omega)_{DHF}$ than $(d\sigma_{el}/d\Omega)_{TFD}$ and thus the cross section corresponding to the DHF potential should be recommended for calculations of the IMFPs.

Second source of uncertainties in the measured IMFPs can be due to the IMFPs assumed for the reference material. Tanuma et al. [40] used the IMFPs for Ni calculated from experimental optical data in an earlier work [46]. In calculations reported here, the IMFPs for Ni were taken from ref. [36]. One should also mention that the reference IMFPs were recommended by Powell and Jablonski [37] for four materials (Ni, Cu, Ag and Au). The IMFPs for nickel from these three sources are compared in Fig. 26. The lower panel shows the percentage differences:

$$\Delta\lambda_{in}^{T-TPP} = 100\frac{\lambda_{in}^{(T)} - \lambda_{in}^{(TPP)}}{\lambda_{in}^{(TPP)}} \qquad \Delta\lambda_{in}^{R-TPP} = 100\frac{\lambda_{in}^{(R)} - \lambda_{in}^{(TPP)}}{\lambda_{in}^{(TPP)}} \tag{47}$$

where $\lambda_{in}^{(T)}$ are the IMFPs for Ni taken from ref. [46], $\lambda_{in}^{(R)}$ are the recommended IMFPs taken from ref. [37], and $\lambda_{in}^{(TPP)}$ are the IMFPs taken from ref. [36] that were used in the present work. Generally agreement between IMFPs for Ni is very good, although the differences of 8% may be expected at 50 eV. This difference is certainly contributing to differences $\Delta\lambda_{in}^{T-MC}$ between the IMFPs from two Monte Carlo codes.

As shown in Table 4, the difference between IMFPs calculated from the two Monte Carlo codes, $< \Delta\lambda_{in}^{T-MC} >$, distinctly decrease, by a factor of almost two, in the energy range from 200 eV to 5000 eV. This energy range should be recommended for determination of IMFPs from the elastic peak intensity. Note that for this energy range, the difference between the IMFPs derived from the analytical formalism and the Monte Carlo simulations is the smallest, i.e. equal to 3.09%. This is distinctly less than the scatter of IMFPs resulting from different Monte Carlo simulation codes. One should also mention that different strategies of Monte Carlo simulation may affect the calculated IMFPs. At energies exceeding 200 eV, the trajectory reversal strategy proposed by Werner [9] may lead to differences up to 5% from a

conventional Monte Carlo strategy used here. Consequently, the analytical formalism analyzed here can be safely used for determination of IMFPs.

The analytical formalism used here is an extension of the formalism proposed by Oswald et al. [11]. The derivation was originally based on the nonrelativistic elastic scattering cross sections. Extension of this theory to relativistic phase shifts was proposed by Dubus et al. [8]. The present extension to alloys and compounds turns out to be very reliable. The IMFPs calculated from the Monte Carlo calculations for these solids are practically reproduced by the IMFPs from the modified analytical formalism. More pronounced differences are between the published IMFPs and the IMFPs determined here. This is due to different theoretical models used in the past: oversimplified electron transport theory [42] or the elastic scattering cross sections from the TFD potential assumed in Monte Carlo calculations [43-45]. Results shown in Figs 23 and 24 additionally justify usefulness of the analytical formalism in EPES calculations.

In the present work, the influence of surface excitations on the elastically backscattered intensity was not considered. Chen et al. [47] has shown that the energy losses during electron crossing of a surface region have a non-negligible effect on the measured intensity. These authors proposed a correction procedure for taking into account the surface excitations in theoretical models simulating the electron trajectories. Simple expressions describing this correction called the surface excitation parameter (SEP) were proposed by Werner et al. [48] and Chen [49]. Parameters needed for these expressions were determined for a limited number of solids [34,48-50]. Werner et al. [48] proposed a predictive formula for SEP applying to medium energy electrons and arbitrary material, although an accuracy of such approach may be rather limited. On the other hand, it has been indicated that the neglect of surface excitations in the procedure of determining the IMFPs from the measured ratio of intensities is a justified practice [37,40]. In a given ratio, the surface excitation effects

partially cancel and the resulting uncertainties in the IMFPs may be negligibly small. Nonetheless, in the present work, the stress is put on evaluation of accuracy of the analytical formalism by comparison with results obtained from Monte Carlo simulations. If we correct for surface excitations the elastically backscattered intensities that result from two theoretical models, the percentage deviation between these intensities would not be affected.

Finally, the database of parameters A_l should be briefly discussed. A very fast performance of an algorithm calculating the elastic backscattering probability requires the pre-calculated set of these parameters. Calculations of parameters A_l with sufficient accuracy for l values reaching the doubled parameter $n_{\max}$ [see Figs 3(a) and (3(b)] requires a considerable computer time. Furthermore, to ensure an accurate interpolation between A_l values from the database to obtain the A_l parameter for the needed energy (see Fig. 5), the database should be prepared for a possibly dense grid of energies. In the present work, the A_l values were calculated for each element for 200 energies uniformly distributed in the logarithmic scale in the range from 50 eV to 5000 eV. Such grid of energies ensures high accuracy of the analytical formalism. A word of caution should also be added here. In a very few cases, the A_l values may be negative. This may occur for in vicinity of the lowest energy considered, i.e. 50 eV. For example, the A_l parameter for chromium and for $l=5$ in the energy range from 50 eV to 54.82 eV increases from -1.7417×10^{-2} to -8.7658×10^{-4}. In that case the interpolation in a doubly-logarithmic coordinates is not possible. The interpolation in the linear coordinates is needed then. However, inasmuch as the determination of IMFPs from ratios of elastic peak intensities is recommended for energies exceeding 200 eV, the problem of negative parameters A_l is not essential.

5. Conclusions

Eq. (1) describing the elastic electron backscattering probability has been shown to have accuracy comparable to Monte Carlo algorithms. Applicability of this equation was extended here to alloys and compounds; the results obtained lead to an analytical algorithm which is potentially useful in elastic peak electron spectroscopy for determination of the IMFP. The summary of these results is the following:

1. A relatively simple expression given by Eq. (1) requires calculations of parameters A_l defined by Eq. (3). A relatively involved algorithm is recommended for this stage of calculations. Furthermore, these calculations require a considerable computer time. However, the parameters A_l are shown to be smooth functions of energy and can be accurately interpolated to obtain values for a given energy. Consequently, we need to calculate a database of A_l parameters for all elements and a reasonably dense grid of energies, and these calculations are performed only once.

2. As follows from Table 4, the average percentage difference between the IMFPs obtained for 13 elemental solids from the Monte Carlo simulations and from the analytical formalism is equal to 4.24% (energy range from 50 eV to 5000 eV) or 3.09% (energy range from 200 eV to 5000 eV). Such deviation is smaller than deviations obtained from two Monte Carlo codes in which different input parameters are used (e.g., elastic scattering cross sections, IMFPs for reference materials).

3. Comparisons of the two theoretical models, the Monte Carlo algorithm and the algorithm based on the analytical formalism were made for experimental configurations in which the normal incidence of the primary beam was assumed, i.e. $\theta_0 = 0°$. In this geometry, both theoretical models provided results in perfect agreement. For this reason, experiments with

normal incidence are recommended for EPES applications. As follows from Figs 7 – 10, a good agreement of the calculated elastically backscattered probabilities is observed in wide range of emission angles, α, up to $\alpha = 85°$. Agreement with experimentally measured backscattered intensities is observed in the range $35° \le \alpha \le 74°$; thus an emission angle from this range is recommended for measurements using EPES. In fact, the IMFP measurements are frequently made using the cylindrical mirror analyzer in which the emission angle is close to 42°.

4. Although the IMFPs from the EPES method were reported for energies down to 50 eV (e.g. refs [38-40]), a safe lower energy limit seems to be close to 200 eV. This conclusion follows from Table 4. In the energy range from 200 eV to 5000 eV, we observe improved agreement between IMFPs from the analytical formalism and the Monte Carlo simulations. Furthermore, the IMFPs from two Monte Carlo codes are also in better agreement. Similar limit of validity of the theoretical model implemented in the Monte Carlo strategy was also suggested by Werner et al. [38,39].

Recently, Bourke and Chantler [51-55] performed detailed analysis of theoretical models describing the IMFPs in the low energy region, i.e. from 1 eV to 120 eV. These authors developed an accurate method for determination of the IMFP from analysis of X-ray absorption fine structure (XAFS) [51-52]. It has been shown that IMFPs calculated from different theoretical models considerably diverge in the low energy region. They also diverge from the IMFPs determined from XAFS. The authors analyzed different possible improvements of theory. Although the presently published set of calculated IMFPs is very limited, this approach seem to be very prospective as a source of these data for the low energy region.

A considerable advantage of the EPES method is due to relatively simple measurements that provide the ratio of elastic peak intensities. If the accompanying

calculations are very fast and accurate, the IMFPs can be determined for a particular sample under study. Furthermore, convenience of such measurements facilitates the determination of IMPFs for numerous areas on a given sample. The energy limit exceeding 200 eV is sufficient for typical analytical applications of X-ray photoelectron spectroscopy (XPS) using instruments equipped with Mg Kα ($h\nu$ = 1253.6 eV) and Al Kα ($h\nu$ = 1486.6 eV) X-ray sources. Hard X-ray photoelectron spectroscopy measurements (HAXPES) can be performed using the laboratory X-ray sources with higher radiation energy: Zr Lα ($h\nu$ = 2042.4 eV), Ag Lα ($h\nu$ = 2984 eV) or Ti Kα ($h\nu$ = 4510 eV). Quantification of XPS and HAXPES requires knowledge of photoelectron IMFPs [56] and thus the upper limit of 5000 eV makes possible to use the analytical algorithm proposed here for such applications. However, it should be noted that most of the HAXPES measurements are performed using synchrotron radiation. It would be important to investigate the validity of the present analytical model in the case of higher (up to 12-15 keV) electron energies, and such studies are planned in the future.

Acknowledgement

The author would like to thank Dr S. Tanuma for providing the numerical values of ratios of elastic backscattering intensities and the corresponding IMFPs.

Appendix

The relation between the parameter A_l and the series of relativistic phase shifts, δ_n^+ and δ_n^-, n = 0, 1, 2, ... , has the following form [8,10]

$$A_l = \frac{1}{\sigma_{el}} \frac{4\pi}{K^2} \left[\sum_{n=0}^{\infty} \sum_{k=0}^{\infty} \Phi_1(l,n,k) \begin{pmatrix} l & n & k \\ 0 & 0 & 0 \end{pmatrix}^2 - \sum_{n=0}^{\infty} \sum_{k=0}^{\infty} \Phi_2(l,n,k) \begin{pmatrix} l & n & k \\ 0 & 1 & -1 \end{pmatrix} \begin{pmatrix} l & n & k \\ 0 & 0 & 0 \end{pmatrix} . \right] \quad \text{(B1)}$$

where

$$\begin{aligned} \Phi_1(l,n,k) = {} & (n+1)(k+1)\cos(\delta_n^+ - \delta_k^+)\sin\delta_n^+ \sin\delta_k^+ \\ & + (n+1)k\cos(\delta_n^+ - \delta_k^-)\sin\delta_n^+ \sin\delta_k^- \\ & + n(k+1)\cos(\delta_n^- - \delta_k^+)\sin\delta_n^- \sin\delta_k^+ \\ & + nk\cos(\delta_n^- - \delta_k^-)\sin\delta_n^- \sin\delta_k^- \end{aligned} \quad \text{(B2)}$$

$$\begin{aligned} \Phi_2(l,n,k) = {} & \cos(\delta_n^+ + \delta_n^- - \delta_k^+ - \delta_k^-)\sin(\delta_n^- - \delta_n^+)\sin(\delta_k^- - \delta_k^+) \\ & \times \left[n(n+1)k(k+1) \right]^{1/2} \end{aligned} \quad \text{(B3)}$$

$\begin{pmatrix} l & n & k \\ 0 & 0 & 0 \end{pmatrix}$ and $\begin{pmatrix} l & n & k \\ 0 & 1 & -1 \end{pmatrix}$ are the Wigner 3j symbols, and K is the wave number of the projectile. Furthermore, the total elastic scattering cross section, σ_{el}, is expressed by the phase shifts

$$\sigma_{el} = \frac{4\pi}{K^2} \sum_{n=0}^{\infty} \left[(n+1)\sin^2(\delta_n^+) + n\sin^2(\delta_n^-) \right] \quad \text{(B4)}$$

The number of summation components in Eq. (B1) is reduced due to the fact that a finite number of phase shifts is available. The index n can vary up to $n_{\max} = N$. Furthermore, due to symmetry properties of the Wigner 3j symbols, the range of index k in Eq. (B1) is reduced to vary between $k_{\min}$ and $k_{\max}$

$$k_{\min} = \begin{cases} |l-n| & \text{if } l \neq n \\ 1 & \text{if } l = n \end{cases} \qquad k_{\max} = \begin{cases} l+n & \text{if } l+n \leq N \\ N & \text{if } l+n > N \end{cases} \tag{B5}$$

Eventually, we obtain

$$A_l = \frac{\sum_{n=0}^{N} \sum_{k=k_{\min}}^{k_{\max}} \Phi_1(l,n,k) \begin{pmatrix} l & n & k \\ 0 & 0 & 0 \end{pmatrix}^2 - \sum_{n=0}^{N} \sum_{k=k_{\min}}^{k_{\max}} \Phi_2(l,n,k) \begin{pmatrix} l & n & k \\ 0 & 1 & -1 \end{pmatrix} \begin{pmatrix} l & n & k \\ 0 & 0 & 0 \end{pmatrix}}{\sum_{n=0}^{N} \left\{ (n+1)\sin^2(\delta_n^+) + n\sin^2(\delta_n^-) \right\}}. \tag{B6}$$

Final reduction of the summation components arises from the fact that the components in the numerator are different from zero only for even values of the sum $l+n+k$. We note that the parameter A_l for any value of index l is a function of the phase shifts only.

References

[1] G. Gergely, Elastic backscattering of electrons: determination of physical parameters of electron transport processes by elastic peak electron spectroscopy, Progress Surface Sci. 71 (2002) 31-88.

[2] A. Jablonski, Analytical applications of elastic electron backscattering from surfaces, Progress Surface Sci. 74 (2003) 357-374.

[3] A. Jablonski and C. J. Powell, Information Depth for Elastic-Peak Electron Spectroscopy, Surface Sci. 551 (2004) 106-124.

[4] A. Jablonski, Elastic backscattering of electrons from surfaces, Surface Sci. 151 (1985) 166-182.

[5] A. Jablonski, J. Gryko, J. Kraaer and S. Tougaard, Elastic electron backscattering from surfaces, Phys. Rev. B39, (1989) 61-71.

[6] A. Jablonski, Elastic electron backscattering from gold, Phys. Rev. B43 (1991) 7546-7554.

[7] B. Tombuyses and A. Dubus, Contribution to the study of elastic backscattering from polycrystalline metallic targets by Monte Carlo simulation, Mathematics and Computers in Simulation 47 (1998) 483-491.

[8] A. Dubus, A. Jablonski and S. Tougaard, Evaluation of theoretical models for elastic electron backscattering from surfaces, Progress Surface Sci. 63 (2000) 135-175.

[9] W. S. M. Werner, Trajectory reversal approach for electron backscattering from solid surfaces, Phys. Rev. B71 (2005) 115415.

[10] A. Jablonski, Angular distribution of elastic electron backscattering from surfaces: determination of the electron inelastic mean free path, J. Phys. D: Appl. Phys. 47 (2014) 055301.

[11] R. Oswald, E. Kasper and K. H. Gaukler, A multiple scattering theory of elastic electron backscattering from amorphous surfaces, J. Electron Spectrosc. Relat. Phenom. 61 (1993) 251-274.

[12] V. M. Dwyer, Angular distribution of electrons elastically backscattered from surfaces, Surface Interface Anal. 20 (1993) 513-518.

[13] W. S. M. Werner, I. S. Tilinin and M. Hayek, Angular distribution of electrons reflected elastically from noncrystalline solid surfaces, Phys. Rev. B50 (1994) 4819-4833.

[14] I. Pazsit and R. Chakarova, Path-length distribution of electrons reflected elastically from solids, Phys. Rev. B50 (1994) 13953-13961.

[15] N. G. Sjöstrand, Angular distribution of elastically backscattered electrons, Surface Interface Anal. 23 (1995) 785-788.

[16] L. G. Glazov and S. Tougaard, Electron backscattering from surfaces: The invariant-embedding approach, Phys. Rev. B68 (2003) 155409.

[17] L. G. Glazov and S. Tougaard, Electron backscattering from surfaces: Azimuth-resolved distributions, Phys. Rev. B72 (2005) 085406

[18] S. J. B. Reed, Electron microprobe analysis, 2nd edition, Cambridge University Press, Cambridge, 1997, p. 193.

[19] A. Jablonski, F. Salvat and C. J. Powell, Comparison of electron elastic-scattering cross sections calculated from two commonly used atomic potentials, J. Phys. Chem. Ref. Data 33 (2004) 409-451.

[20] F. Salvat, A. Jablonski and C. J. Powell, ELSEPA - Dirac partial-wave calculation of elastic scattering of electrons and positrons by atoms, positive ions and molecules, Comp. Phys. Commun. 165 (2005) 157-190.

[21] Web address: http://cpc.cs.qub.ac.uk/cpc/summaries/ADUS

[22] A. Jablonski, F. Salvat, C. J. Powell, NIST Electron Elastic-Scattering Cross-Section Database, Version 3.2, Standard Reference Data Program Database 64, U.S. Department of Commerce, National Institute of Standards and Technology, Gaithersburg, MD (2010); web address: http://www.nist.gov/srd/nist64.cfm.

[23] I. S. Gradshteyn and I. M. Ryzhik, Table of integrals, series, and products, 7th edition, Elsevier, Amsterdam, 2007, p. 975.

[24] S. Goudsmit and J. L. Saunderson, Multiple scattering of electrons, Phys. Rev. 57 (1940) 24-29.

[25] A. Jablonski, Quantitative AES: Via the inelastic mean free path or the attenuation length?, Surface Interface Anal. 15 (1990) 559-566.

[26] J. Zemek, P. Jiricek, S. Hucek, A. Jablonski and B. Lesiak, Escape probability of photoelectrons from silver sulphide, Surface Sci. 473 (2001) 8-16.

[27] S. Tanuma, C. J. Powell and D. R. Penn, Calculations of electron inelastic mean free paths. V. Data for 14 organic compounds over the 50-2000 eV range, 21 (1994) 165-176.

[28] C. J. Powell C J and A. Jablonski, NIST Electron Inelastic-Mean-Free-Path Database, Version 1.2, Standard Reference Data Program Database 71, US Department of Commerce, National Institute of Standards and Technology, Gaithersburg, MD (2010) web address: http://www.nist.gov/srd/nist71.cfm

[29] J. S. Schilling and M. B. Webb, Low-energy electron diffraction from liquid Hg: Multiple scattering, scattering factor, and attenuation, Phys. Rev. B2 (1970) 1665-1676.

[30] A. Jablonski, H. S. Hansen, C. Jansson and S. Tougaard, Elastic electron backscattering from surfaces with overlayers, Phys. Rev. B45 (1992) 3694-3702.

[31] W. S. M. Werner, I. S. Tilinin and M. Hayek, Angular distribution of electrons

reflected elastically from noncrystalline solid surfaces, Phys. Rev. B50 (1994) 4919-4833.

[32] A. Jablonski and P. Jiricek, Surface Sci., Dependence of experimentally determined inelastic mean free paths of electrons on the measurement geometry, Surface Sci. 412/413 (1998) 42-54.

[33] A. Jablonski and J. Zemek, Angle-resolved elastic-peak electron spectroscopy: Solid-state effects, Surface Sci. 600 (2006) 4464-4474.

[34] A. Jablonski and J. Zemek, Angle-resolved elastic peak electron spectroscopy: Role of surface excitations, Surface Sci. 601 (2007) 3409-3420.

[35] A. Jablonski and J. Zemek, Remarks on some reference materials for applications in elastic peak electron spectroscopy, Analytical Sci. 26 (2010) 239-246.

[36] S. Tanuma, C. J. Powell and D. R. Penn, Calculations of electron inelastic mean free paths. IX. Data for 41 elemental solids over the 50 eV to 30 keV range, Surface Interface Anal. 43 (2011) 689-713.

[37] C. J. Powell and A. Jablonski, Evaluation of calculated and measured electron inelastic mean free paths near solid surfaces, J. Phys. Chem. Ref. Data 28, (1999) 19-62.

[38] W. S. M. Werner, C. Tomastic, T. Cabela, G. Richter and H. Störi, Electron inelastic mean free path measured by elastic peak electron spectroscopy for 24 solids between 50 and 3400 eV, Surface Sci. 470 (2000) L123-L128.

[39] W. S. M. Werner, C. Tomastic, T. Cabela, G. Richter and H. Störi, Elastic electron reflection for determination of the inelastic mean free path of medium energy electrons in 24 elemental solids for energies between 50 and 3400 eV, J. Electron Spectrosc. Relat. Phenom. 113 (2001) 127-135.

[40] S. Tanuma, T. Shiratori, T. Kimura, K. Goto, S. Ichimura and C. J. Powell,

Experimental determination of electron inelastic mean free paths in 13 elemental solids in the 50 to 5000 eV energy range by elastic-peak electron spectroscopy, Surface Interface Anal. 37 (2005) 833-845.

[41] Y. Takeichi and K. Goto, True Auger electron spectra measured with a novel cylindrical mirror analyzer (Au, Ag, and Cu), Surface Interface Anal. 25 (1997) 17-24.

[42] P. Mrozek, A. Jablonski and A. Sulyok, The inelastic mean free path of electrons in the ordered $Al_{48}Ni_{52}$ alloy, Surface Interface Anal. 11 (1988) 499-501.

[43] G. Gergely, A. Sylyok, M. Menyhard, J. Toth, D. Varga, A. Jablonski, M. Krawczyk, B. Gruzza, L. Bideux and C. Roberts, Experimental determination of inelastic mean free path of electrons in GaSb and InSb, Appl. Surface Sci. 144-145 (1999) 173-177.

[44] M. Krawczyk, L. Zommer, A. Jablonski, I. Grzegory and M. Bockowski, Energy dependence of electron inelastic mean free paths in bulk GaN crystals, Surface Sci. 566-568 (2004) 1234-1239.

[45] M. Krawczyk, L. Zommer, A. Kosinski, J. W. Sobczak and A. Jablonski, Measured electron IMFPs for SiC, Surface Interface Anal. 38 (2006) 644-647.

[46] S. Tanuma, S. Ichimura and K. Goto, Estimation of surface excitation correction factor for 200-5000 eV in Ni from absolute elastic scattering electron spectroscopy, 30 (2000) 212-216.

[47] Y. F. Chen, P. Su, C. M. Kwei and C. J. Tung, Influence of surface excitations on electrons elastically backscattered from copper and silver surfaces, Phys. Rev. B50 (1994) 17547-17555.

[48] W. S. M. Werner, W. Smekal, C. Tomastik and H. Störi, Surface excitation probability of medium energy electrons in metals and semiconductors, Surface Sci. 486 (2001) L461-L466.

[49] Y. F. Chen, Surface effects on angular distributions in X-ray-photoelectron

spectroscopy, Surface Sci. 519 (2002) 115-124.

[50] W. S. M. Werner, L. Kövér, S. Egri, J. Tóth and D. Varga, Measurement of the surface excitation probability of medium energy electrons reflected from Si, Ni, Ge and Ag surfaces, Surface Sci. 585 (2005) 85-94.

[51] J. D. Bourke and C. T. Chantler, Measurements of electron inelastic mean free paths in materials, Phys. Rev. Lett. 104(2010) 206601.

[52] C. T. Chantler and J. D. Bourke, X-ray spectroscopic measurement of photoelectron inelastic mean free paths in molybdenum, J. Phys. Chem. Lett. 1 (2010) 2422-2427.

[53] J. D. Bourke and C. T. Chantler, Electron energy loss spectra and overestimation of inelastic mean free paths in many pole models, J. Phys. Chem. A116 (2012) 3202-3205.

[54] C. T. Chantler and J. D. Bourke, Full-potential theoretical investigations of electron inelastic mean free paths and extended X-ray absorptionfine structure in molybdenum, J. Phys. Condens. Matter 26 (2014) 145401.

[55] J. D. Bourke and C. T. Chantler, Momentum-dependent lifetime broadening of electron energy loss spectra: A self-consistent copupled-plasmon model, J. Phys. Chem. Lett. 6 (2015) 314-319.

[56] A. Jablonski, Angular distribution of photoelectrons emitted by the laboratory soft and hard X-ray radiation sources, J. Electron Spectrosc. Relat. Phenom. 189(2013) 81-95.

Table 1.

Mean percentage deviations, R_{AN}, and the averaged mean percentage deviations, $< R_{AN} >$, between measured backscattered intensities, $I^{(\exp)}$, and elastic backscattering probabilities calculated from the analytical formalism , $\Delta\eta^{(AN)}$. For each element, the calculated values were fitted to experimental data by selecting an appropriate coefficient C [see Eqs (35) and (37)].

Element	Mean percentage deviation, R_{AN} (%)			
	200 eV	500 eV	1000 eV	$< R_{AN} >$
Silicon	4.42	7.12	9.63	7.06
Iron	15.76	10.03	9.69	11.83
Cobalt	16.38	3.82	3.18	7.79
Nickel	16.67	3.77	3.52	7.99
Copper	17.56	16.07	8.66	14.10
Palladium	11.22	11.86	5.87	9.65
Silver	7.73	5.49	6.40	6.54
Samarium	5.89	7.87	7.10	6.97
Iridium	11.70	5.54	8.56	8.60
Gold	8.20	9.92	5.63	7.92
Total mean	11.55	8.15	6.82	8.84

Table 2.

Mean percentage deviations, R_{MC}, and the averaged mean percentage deviations, $< R_{MC} >$, between measured backscattered intensities, $I^{(\mathrm{exp})}$, and elastic backscattering probabilities calculated from Monte Carlo simulations, $\Delta\eta^{(MC)}$. For each element, the calculated values were fitted to experimental data by selecting an appropriate coefficient *C*.

Element	Mean percentage deviation, R_{MC} (%)			
	200 eV	500 eV	1000 eV	$< R_{MC} >$
Silicon	3.22	5.78	7.62	5.54
Iron	14.35	9.01	7.93	10.43
Cobalt	12.57	3.69	1.17	5.81
Nickel	13.31	3.16	1.52	6.00
Copper	14.92	15.80	7.48	12.73
Palladium	7.35	7.51	3.55	6.13
Silver	4.25	4.49	4.72	4.49
Samarium	4.30	2.07	4.55	3.75
Iridium	6.00	3.74	4.20	4.65
Gold	4.10	11.72	4.79	6.87
Total mean	8.44	6.70	4.75	6.64

Table 3.

Mean percentage differences calculated from Eq (41) between theoretical and experimental ratios of elastic backscattering probabilities ($<\Delta\Gamma^{T-AN}>$ and $<\Delta\Gamma^{T-MC}>$) and between ratios resulting from two theoretical models ($<\Delta\Gamma^{MC-AN}>$).

Element	Mean percentage deviations (%)		
	$<\Gamma^{T-AN}>$	$<\Gamma^{T-MC}>$	$<\Gamma^{MC-AN}>$
Graphite	30.13	28.19	7.96
Silicon	14.58	11.85	9.26
Chromium	8.36	7.35	2.49
Iron	12.21	11.81	1.33
Copper	9.90	9.79	0.67
Zinc	14.75	15.24	2.02
Gallium	11.90	13.02	2.55
Molybdenum	15.57	17.40	4.45
Silver	23.64	22.25	3.73
Tantalum	11.00	9.97	6.42
Tungsten	22.16	25.90	6.28
Platinum	17.04	19.37	5.16
Gold	16.63	16.33	5.68
Total mean	15.99	16.04	4.46

Table 4.

Mean percentage differences calculated from Eq (44) between the IMFPs published by Tanuma et al. [40] and the IMFPs determined in the present work ($<\Delta\lambda_{in}^{T-AN}>$ and $<\Delta\lambda_{in}^{T-MC}>$). In the last column, the mean percentage differences are listed due to two theoretical models used here ($<\Delta\lambda_{in}^{MC-AN}>$). The averaging procedure was extended over two energy ranges: from 50 eV to 5000 eV and form 200 eV to 5000 eV.

Element	Mean percentage deviations (%)		
	$<\Delta\lambda_{in}^{T-AN}>$	$<\Delta\lambda_{in}^{T-MC}>$	$<\Delta\lambda_{in}^{MC-AN}>$
Energy range from 50 eV to 5000 eV			
Graphite	15.28	11.68	7.63
Silicon	19.17	15.18	9.11
Chromium	6.92	5.89	2.27
Iron	4.71	4.32	1.72
Copper	4.01	3.76	1.02
Zinc	6.30	5.83	1.74
Gallium	7.98	7.01	2.79
Molybdenum	14.26	15.29	4.70
Silver	12.98	11.14	3.69
Tantalum	13.00	12.26	5.76
Tungsten	12.24	11.12	5.34
Platinum	11.24	9.41	4.38
Gold	13.31	9.60	4.99
Total mean	10.88	9.42	4.24

Table 4.

(Continued)

Element	Mean percentage deviations (%)		
	$< \Delta\lambda_{in}^{T-AN} >$	$< \Delta\lambda_{in}^{T-MC} >$	$< \Delta\lambda_{in}^{MC-AN} >$
Energy range from 200 eV to 5000 eV			
Graphite	4.52	3.97	3.81
Silicon	6.86	5.41	2.10
Chromium	4.60	3.71	1.66
Iron	3.56	3.05	1.31
Copper	2.85	2.88	0.84
Zinc	4.48	4.04	1.57
Gallium	4.41	3.33	2.07
Molybdenum	4.12	5.83	4.15
Silver	8.92	6.64	4.49
Tantalum	14.46	10.80	4.51
Tungsten	13.57	9.69	4.30
Platinum	9.94	7.07	4.02
Gold	12.88	8.02	5.40
Total mean	7.32	5.73	3.09

Figure Captions

Fig. 1. Scheme of the experimental configuration for measurements of the elastic peak intensity and the notation used

Fig. 2. The model trajectory illustrating assumptions of the theory of Oswald et al. [11].

Fig. 3. (Upper panel) The maximum number of relativistic phase shifts, δ_n^+ and δ_n^-, obtained from the ELSEPA program [20,21] for selected elements in the energy range from 50 eV to 5000 eV; (lower panel) the maximum number of relativistic phase shifts at energy of 5000 eV for all elements.

Fig. 4. The 3D plot showing the dependence of the parameter A_l for gold on energy and the coefficient *l*.

Fig. 5. Dependence of the parameter A_l for gold on energy for the first ten coefficients *l*. (a) $1 \le l \le 5$;(b) $6 \le l \le 10$. The curves are identified in the legend in the plots.

Fig. 6. Scheme of elastic collisions on two different scattering centres A and B, and the notation used.

Fig. 7. Comparison of elastically backscattered signal intensity, $I^{(\exp)}$, for nickel with the fitted elastic backscattering probability calculated from different theoretical models, $C\Delta\eta$.

Circles: experimental data; solid line: the analytical formalism; dotted line: the Monte Carlo simulations. (a) Energy of 200 eV; (b) 500 eV; (c) 1000 eV. The mean percentage differences R_{AN} and R_{MC} are also shown in each panel [Cf. Eqs (35) and (36)].

Fig. 8. The same as Fig. 7 except for copper.

Fig. 9. The same as Fig. 7 except for silver.

Fig. 10. The same as Fig. 7 except for gold.

Fig. 11. Comparison of the energy dependence of measured ratios of elastically backscattered signal intensity for an elemental sample and the nickel reference, $I^{(\exp)} / I_{Ni}^{(\exp)}$, with calculated ratios of elastic backscattering probability, $\Delta\eta / \Delta\eta_{Ni}$. Circles: experimental data taken from ref. [40]; solid line: the analytical formalism; dotted line: the Monte Carlo simulations. (a) Graphite; (b) silicon; (c) chromium; (d) iron.

Fig. 12. The same as Fig. 11 except for copper, zinc, gallium molybdenum and silver.

Fig. 13. The same as Fig. 11 except for tantalum, tungsten, platinum and gold.

Fig. 14. The percentage deviations between ratios of elastic backscattering probabilities. Triangles: deviation between experimental ratios and the ratios from the analytical model, $\Delta\Gamma^{T-AN}$ [Eq. (40a)]; empty circles: deviation between experimental ratios and ratios from

Monte Carlo simulations, $\Delta\Gamma^{T-MC}$ [Eq. (40b)]; filled circles: deviation between ratios from two theoretical models, $\Delta\Gamma^{MC-AN}$ [Eq. (40c)]. (a) Graphite; (b) silicon; (c) chromium; (d) iron.

Fig. 15. The same as Fig. 14 except for copper, zinc, gallium, molybdenum and silver.

Fig. 16. The same as Fig. 14 except for tantalum, tungsten, platinum and gold.

Fig. 17. Comparison of the IMFPs obtained from measured ratios of elastic peak intensities using different algorithms. Solid circles: values determined from Monte Carlo simulations by Tanuma et al. [40]; open circles: values obtained in the present work from Monte Carlo simulations; triangles: values obtained from the analytical formalism. Solid line shows energy dependence of IMFPs calculated from experimental optical data [36]. (a) Graphite; (b) silicon; (c) chromium; (d) iron.

Fig. 18. The same as Fig. 17 except for copper, zinc, gallium, molybdenum and silver.

Fig. 19. The same as Fig. 17 except for tantalum, tungsten, platinum and gold.

Fig. 20. The percentage deviations between IMFPs calculated from measured ratios of elastic peak intensities using different algorithms. Triangles: deviations between IMFPs calculated by Tanuma et al. [40] and the IMFPs calculated here from the analytical formalism, $\Delta\lambda_{in}^{T-AN}$ [Eq. (43a)]; open circles: deviations between IMFPs calculated by Tanuma et al. [40] and the IMFPs calculated here from the Monte Carlo simulations, $\Delta\lambda_{in}^{T-MC}$ [Eq. (43b)]; filled circles:

deviation between IMFPs from two theoretical models considered here, $\Delta\lambda_{in}^{MC-AN}$ [Eq. (43c)]. (a) Graphite; (b) silicon; (c) chromium; (d) iron.

Fig. 21. The same as Fig. 20 except for copper, zinc, gallium, molybdenum and silver.

Fig. 22. The same as Fig. 20 except for tantalum, tungsten, platinum and gold.

Fig. 23. Comparison of the IMFPs for compounds obtained from measured ratios of elastic peak intensities. Filled circles: Values taken from published reports; open circles: values calculated here from Monte Carlo simulations; triangles: values calculated here from the analytical formalism. Solid line shows energy dependence of IMFPs calculated from predictive formula TPP-2M [27]. (a) $Al_{0.48}Ni_{0.52}$ alloy; [42]; (b) gallium antimonide, GaSb [43]; (c) indium antimonide, InSb [43]; (d) gallium nitride, $Ga_{0.7}N_{0.3}$ [44]; (e) silicon carbide, SiC [45].

Fig. 24. The percentage deviations between IMFPs calculated for compounds using different algorithms. Triangles: deviations between published IMFPs and the IMFPs calculated here from the analytical formalism, $\Delta\lambda_{in}^{PUBL-AN}$ [Eq. (45a)]; open circles: deviations between published IMFPs and the IMFPs calculated here from the Monte Carlo simulations, $\Delta\lambda_{in}^{PUBL-MC}$ [Eq. (45b)]; filled circles: deviation between IMFPs from two theoretical models considered here, $\Delta\lambda_{in}^{MC-AN}$. (a) $Al_{0.48}Ni_{0.52}$ alloy; [42]; (b) gallium antimonide, GaSb [43]; (c) indium antimonide, InSb [43]; (d) gallium nitride, $Ga_{0.7}N_{0.3}$ [44]; (e) silicon carbide, SiC [45].

Fig. 25. (Upper panels) Differential elastic scattering cross sections, $d\sigma_{el}/d\Omega$, calculated for 50 eV as a function of scattering angle, θ. Solid line: the DHF potential; dashed line: the TFD potential. (Lower panels): Percentage differences between differential elastic scattering cross sections, ΔDCS [Eq. (46)]. (a) Carbon; (b) silicon; (c) molybdenum.

Fig. 26. (Upper panel) Comparison of the IMFPs for Ni used as the reference data. Solid line: IMFPs calculated from experimental optical data [36]; dotted line: recommended IMFPs [28,37]; circles: reference IMFPs used by Tanuma et al. [40]. (Lower panel) Percentage differences between IMFPs for Ni. Dotted line: deviation between IMFPs from experimental optical data and the recommended IMFPs, $\Delta\lambda_{in}^{R-TPP}$; circles: deviations between IMFPs from experimental optical data and the IMFPs used by Tanuma et al. [40], $\Delta\lambda_{in}^{T-TPP}$ [see Eq. (47)].

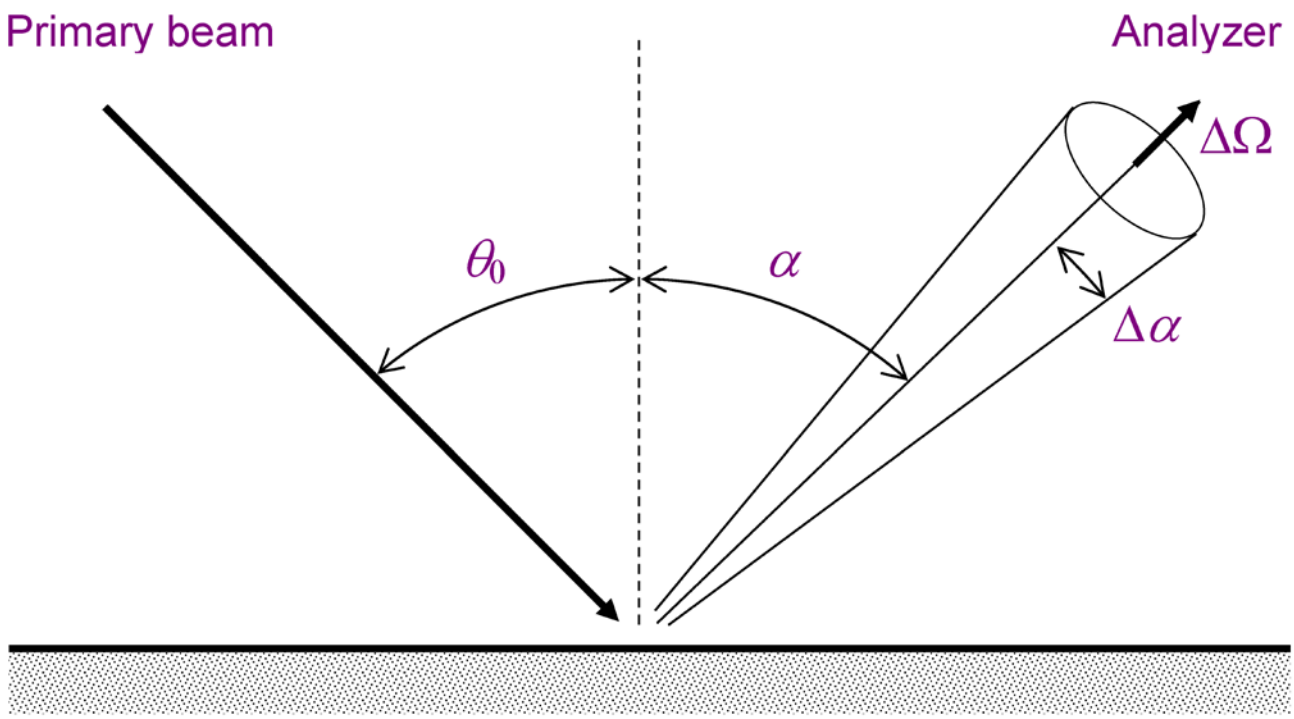

Fig. 1

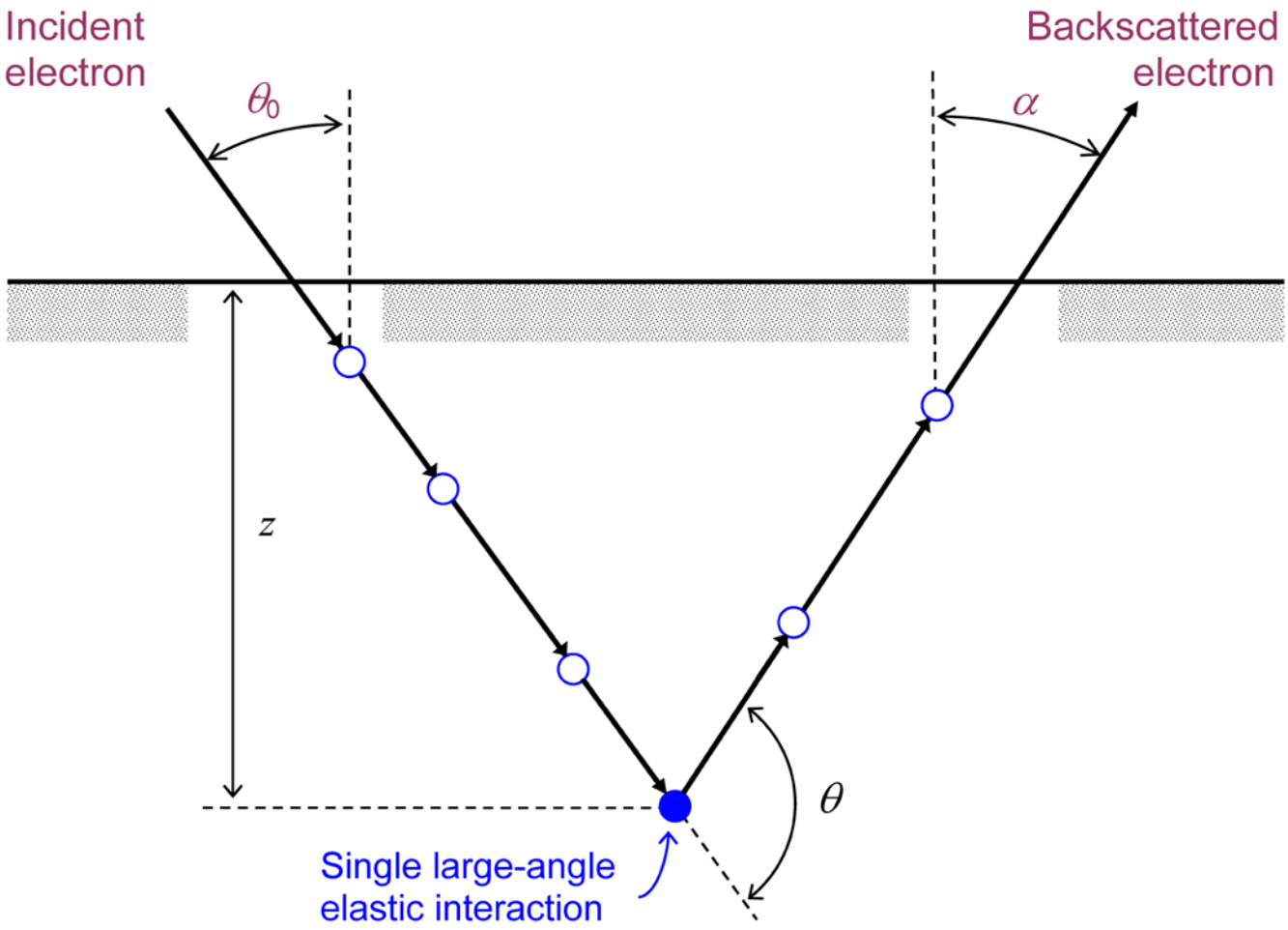

Fig. 2

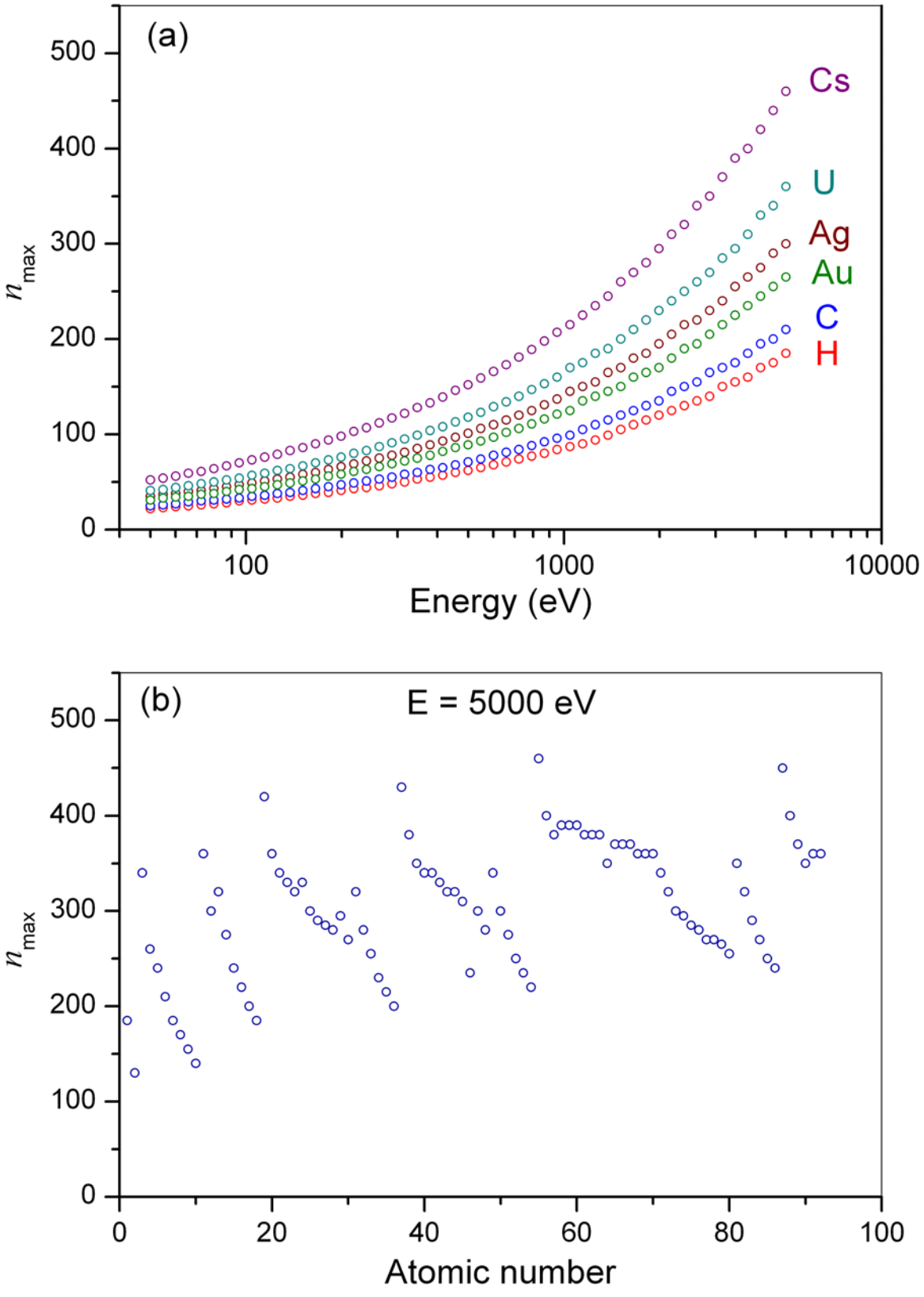

Fig. 3

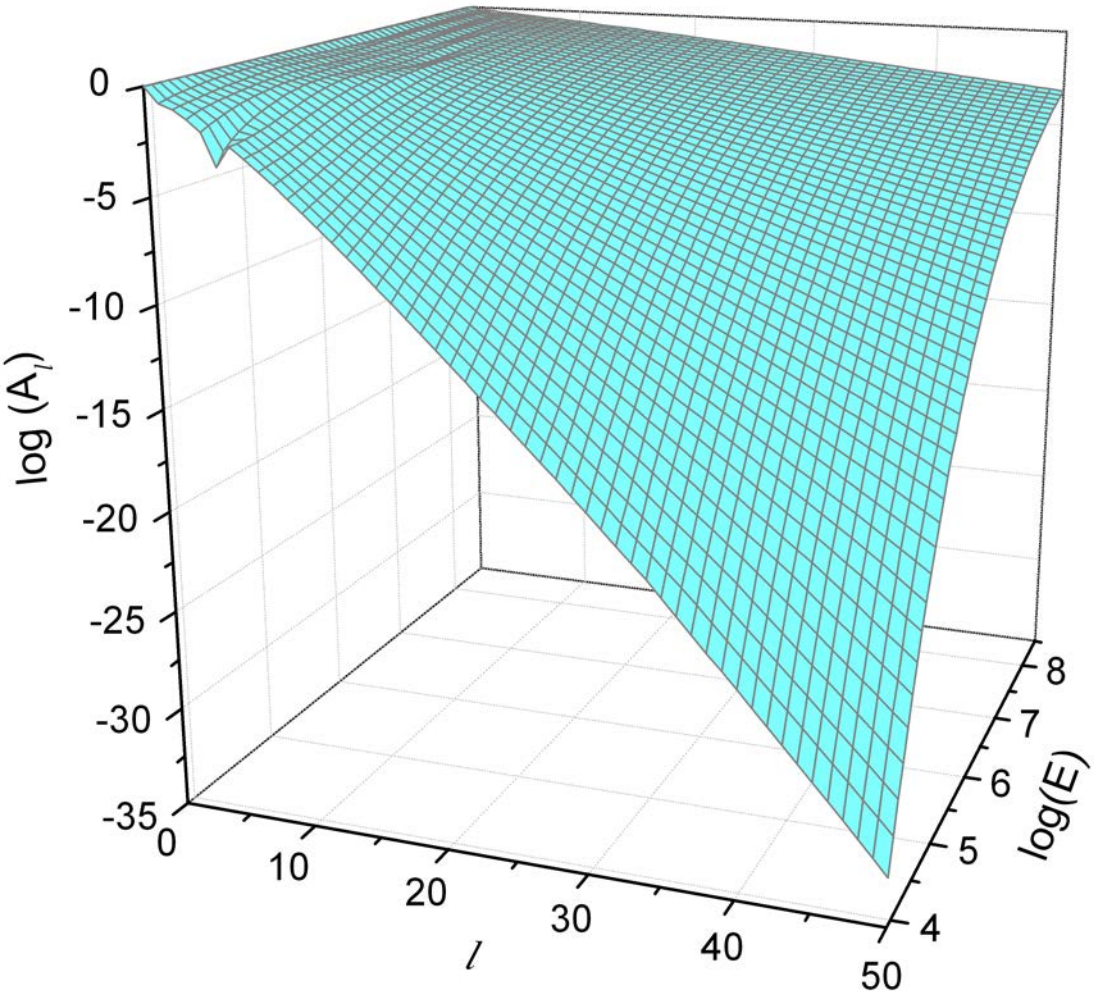

Fig. 4

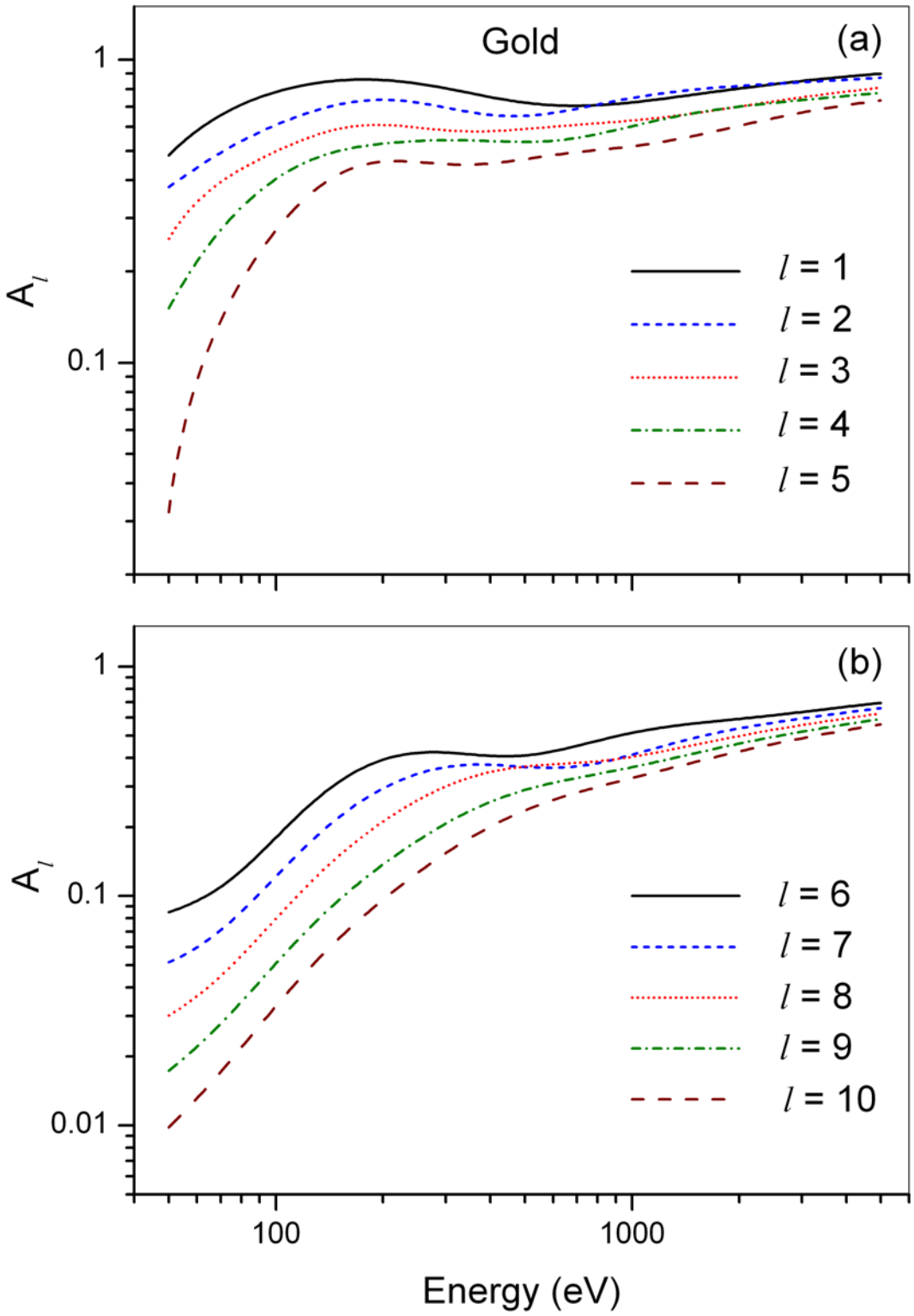

Fig. 5

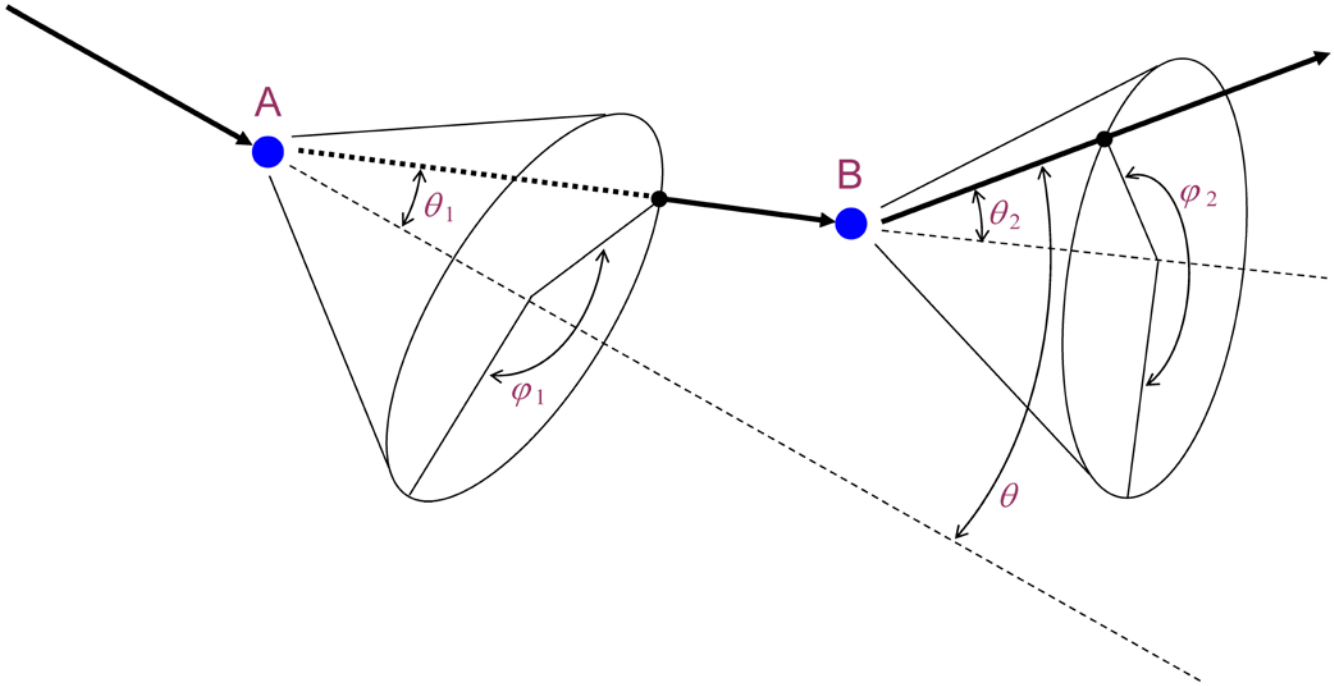

Fig. 6

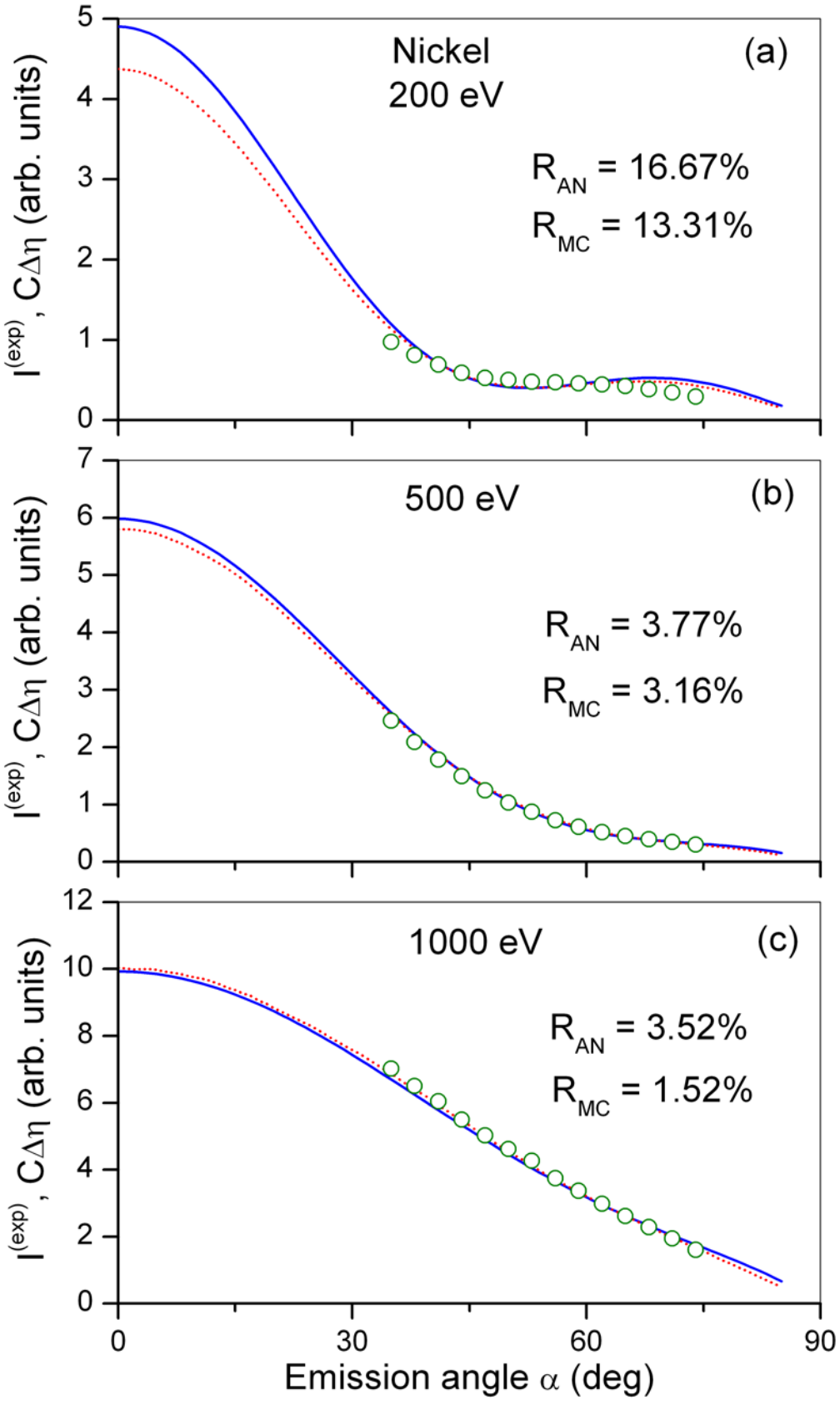

Fig. 7

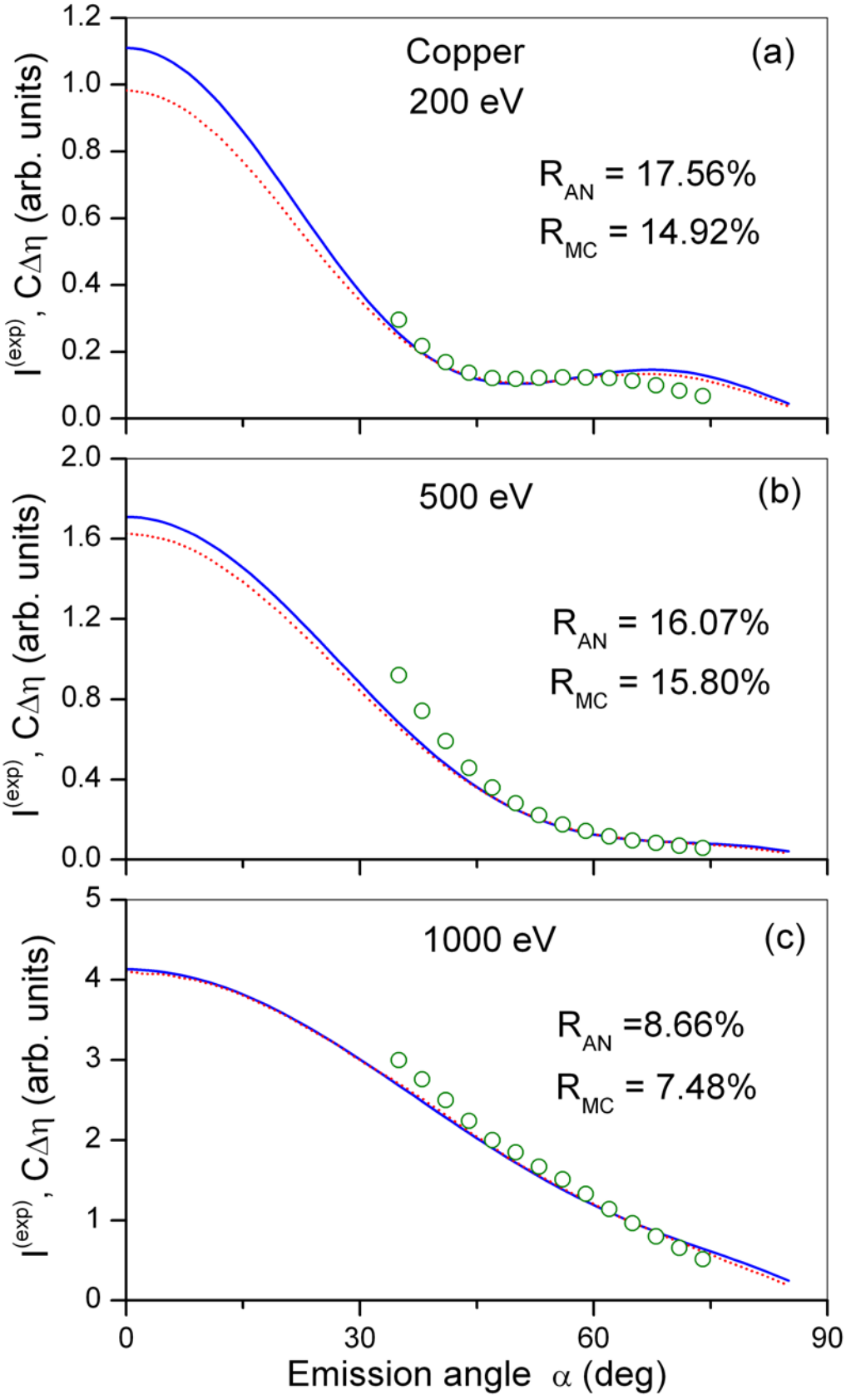

Fig. 8

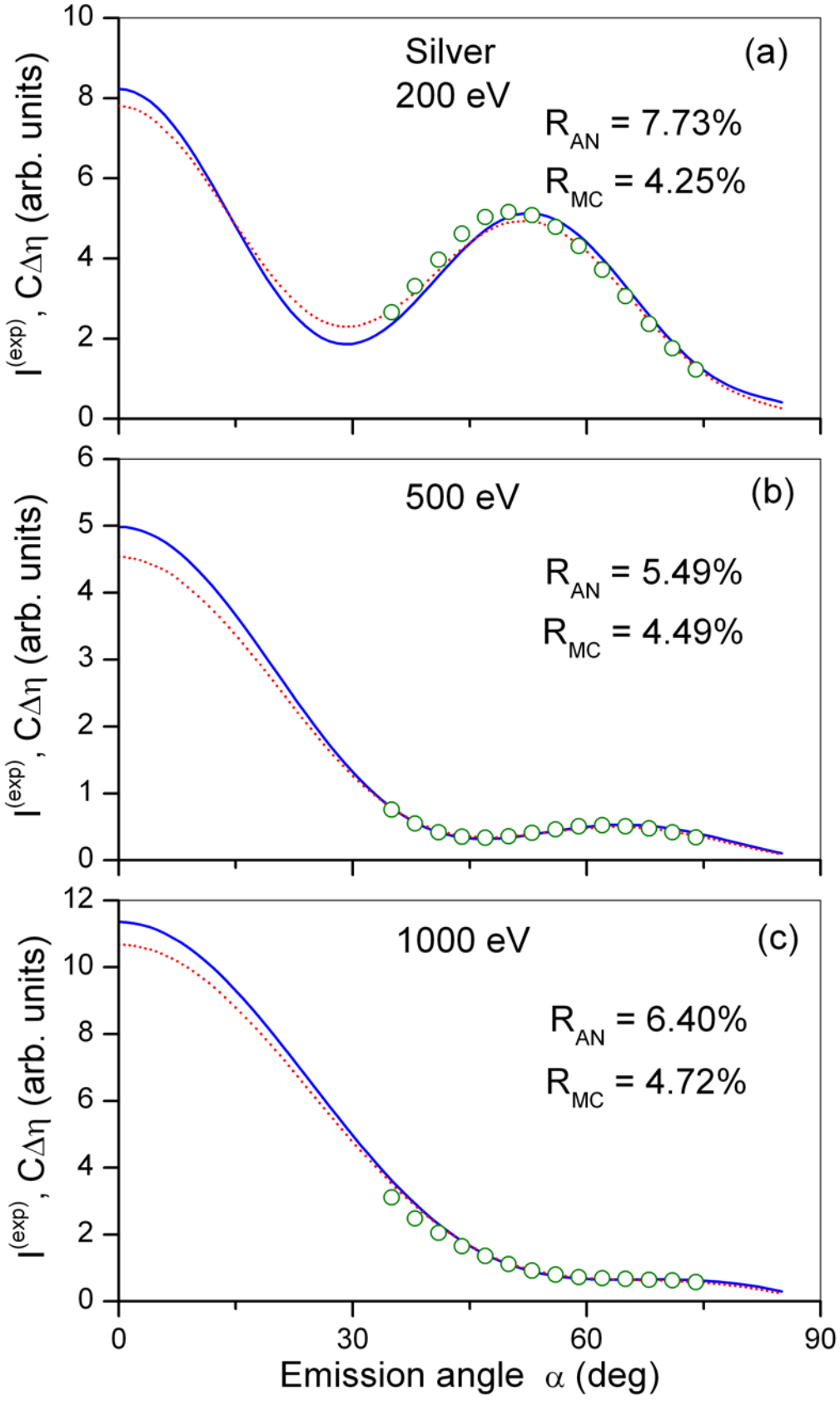

Fig. 9

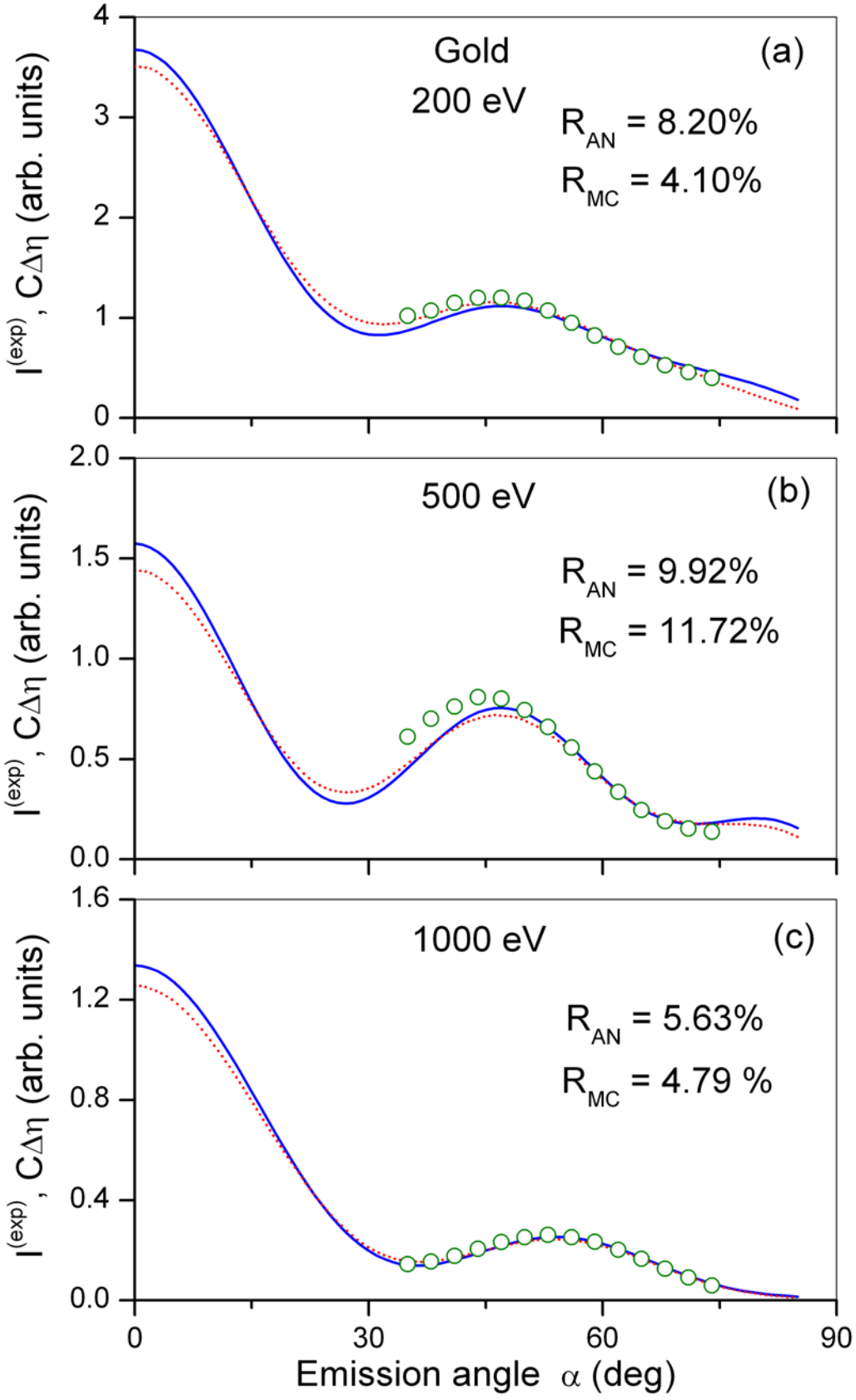

Fig. 10

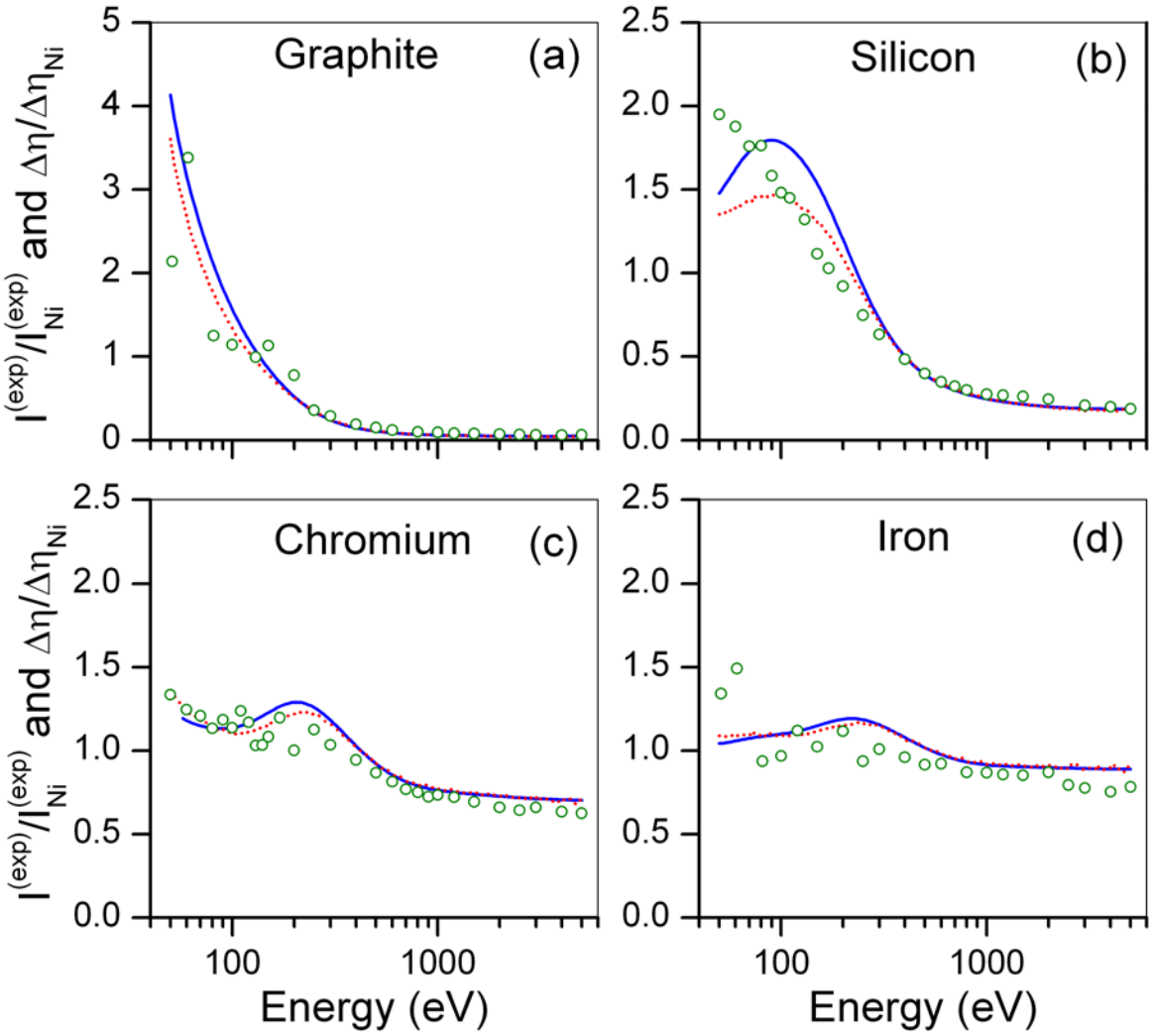

Fig. 11

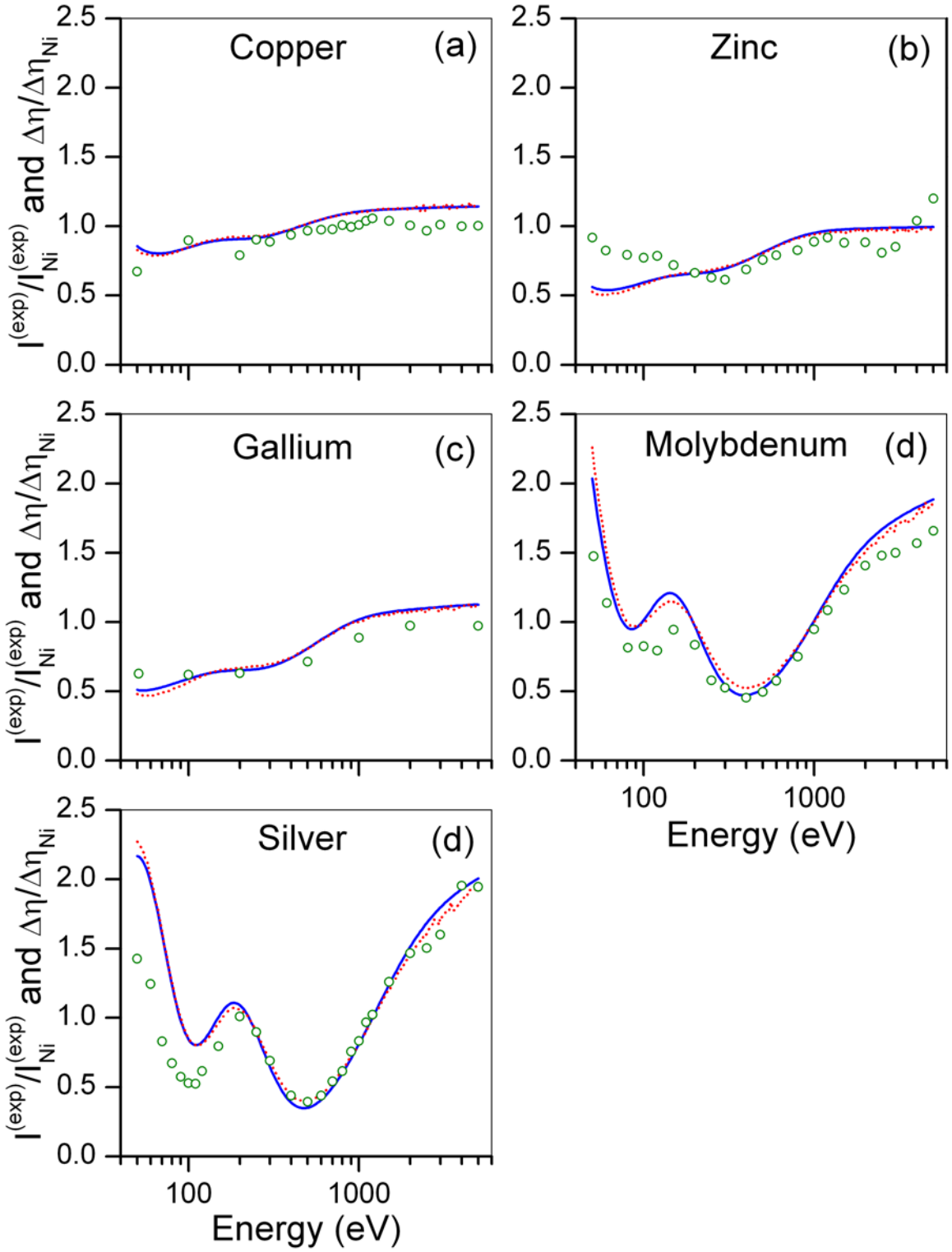

Fig. 12

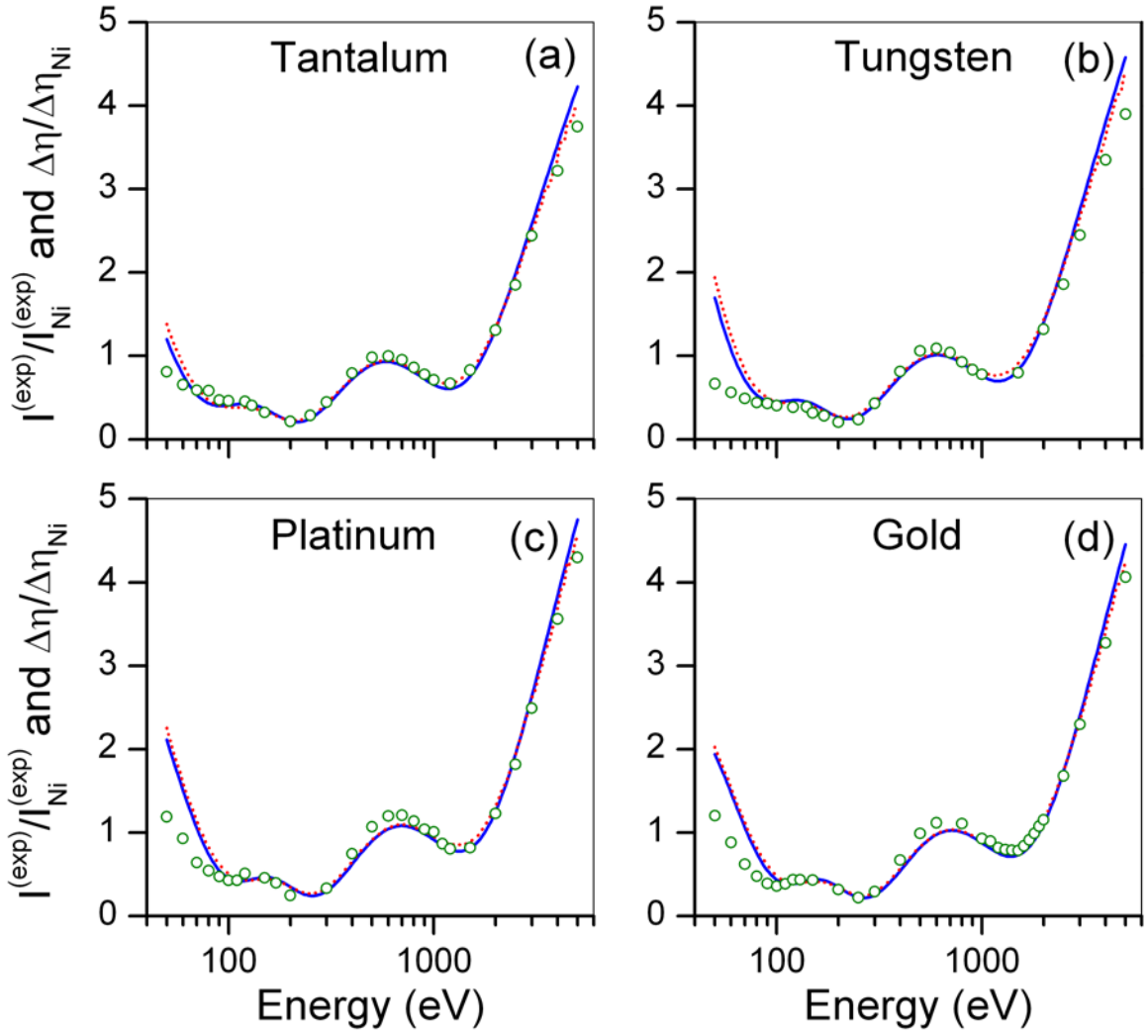

Fig. 13

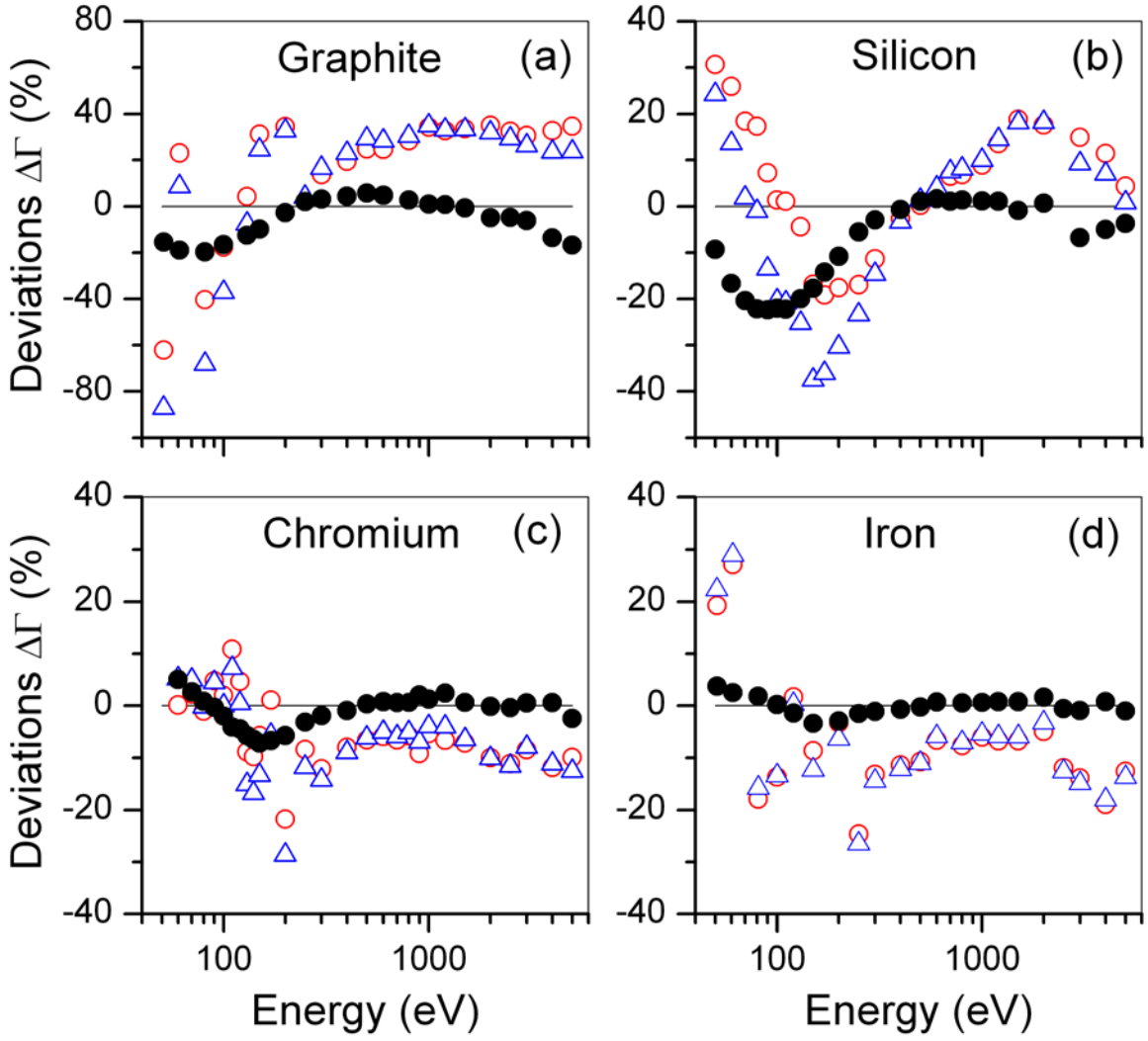

Fig. 14

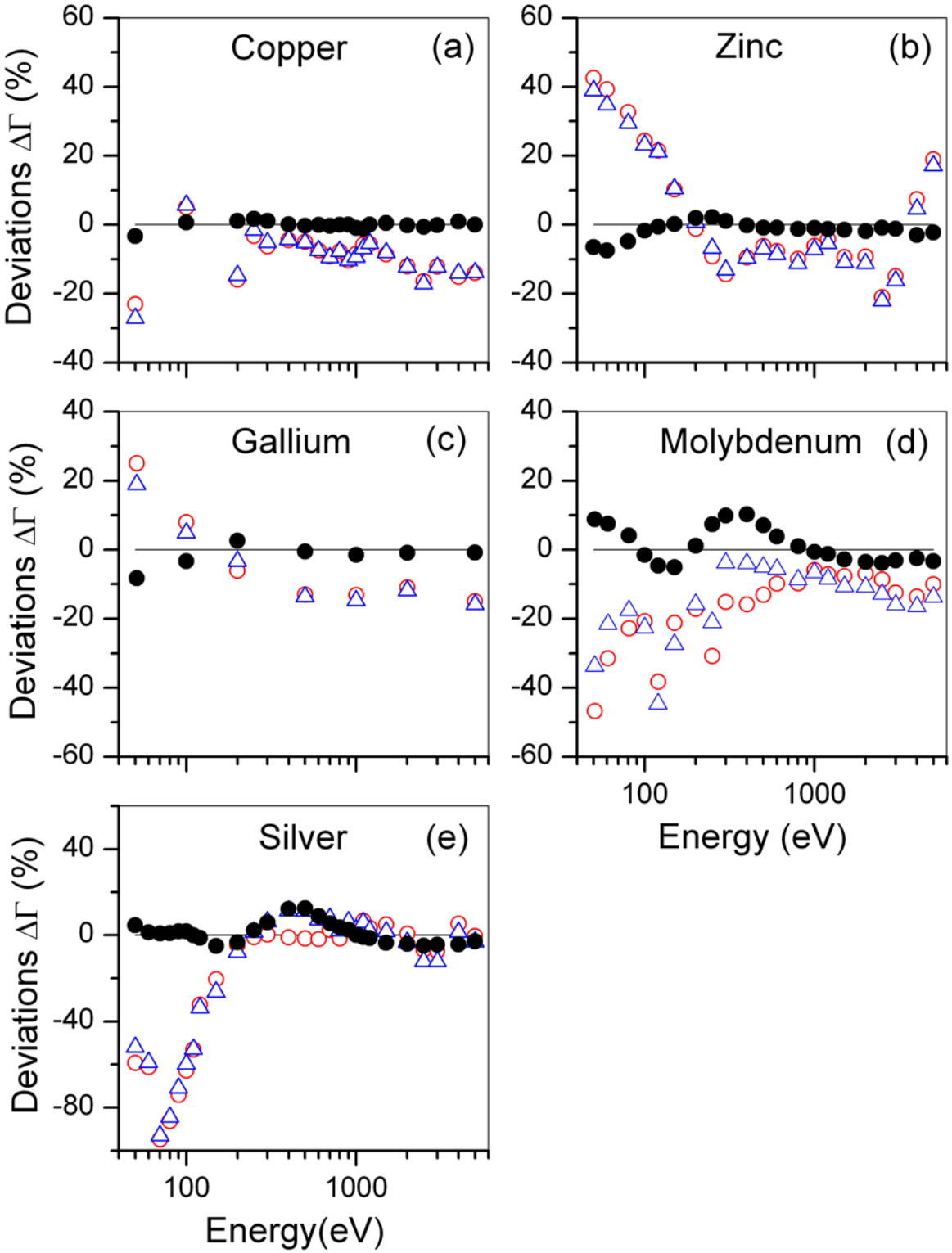

Fig. 15

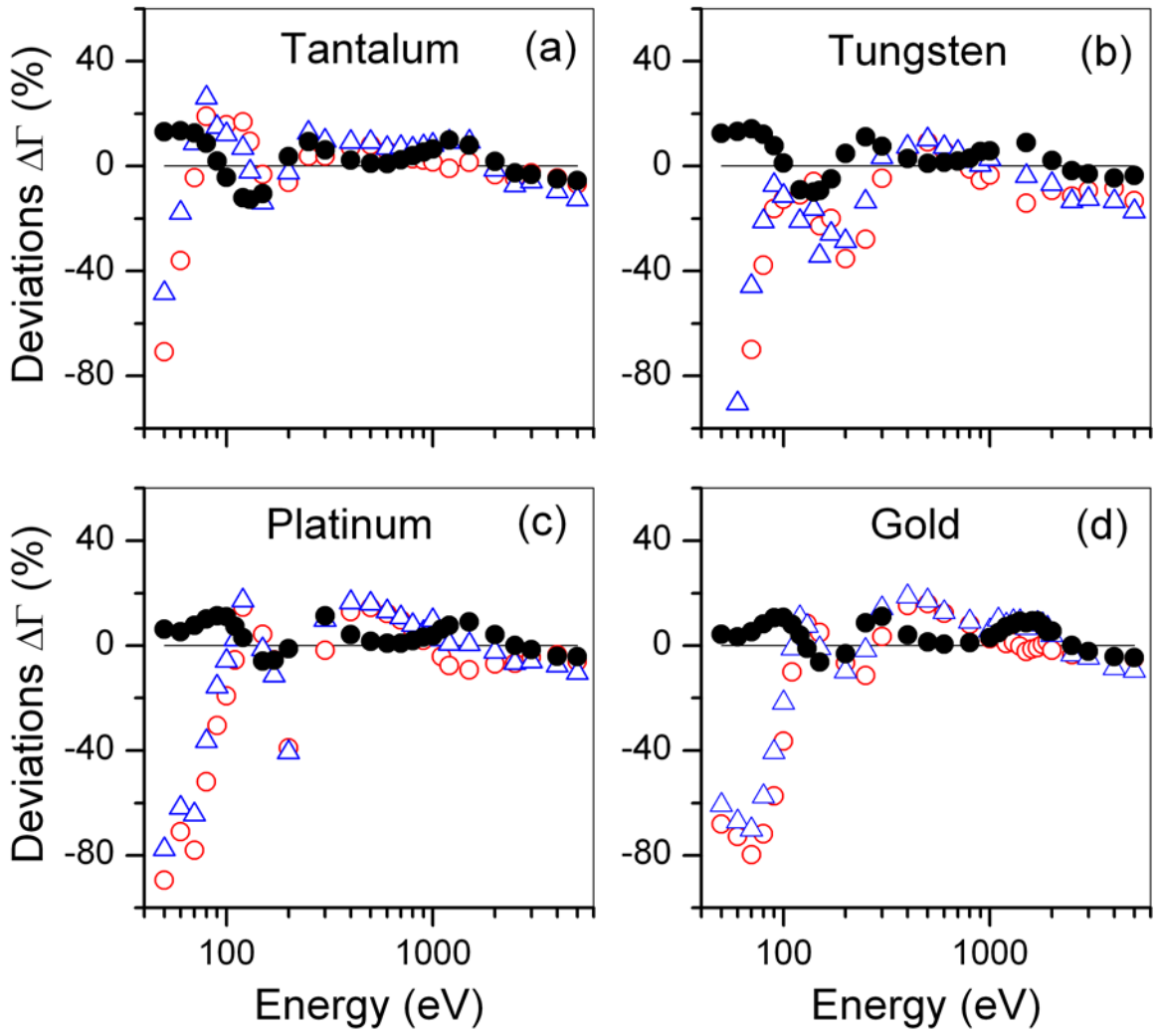

Fig. 16

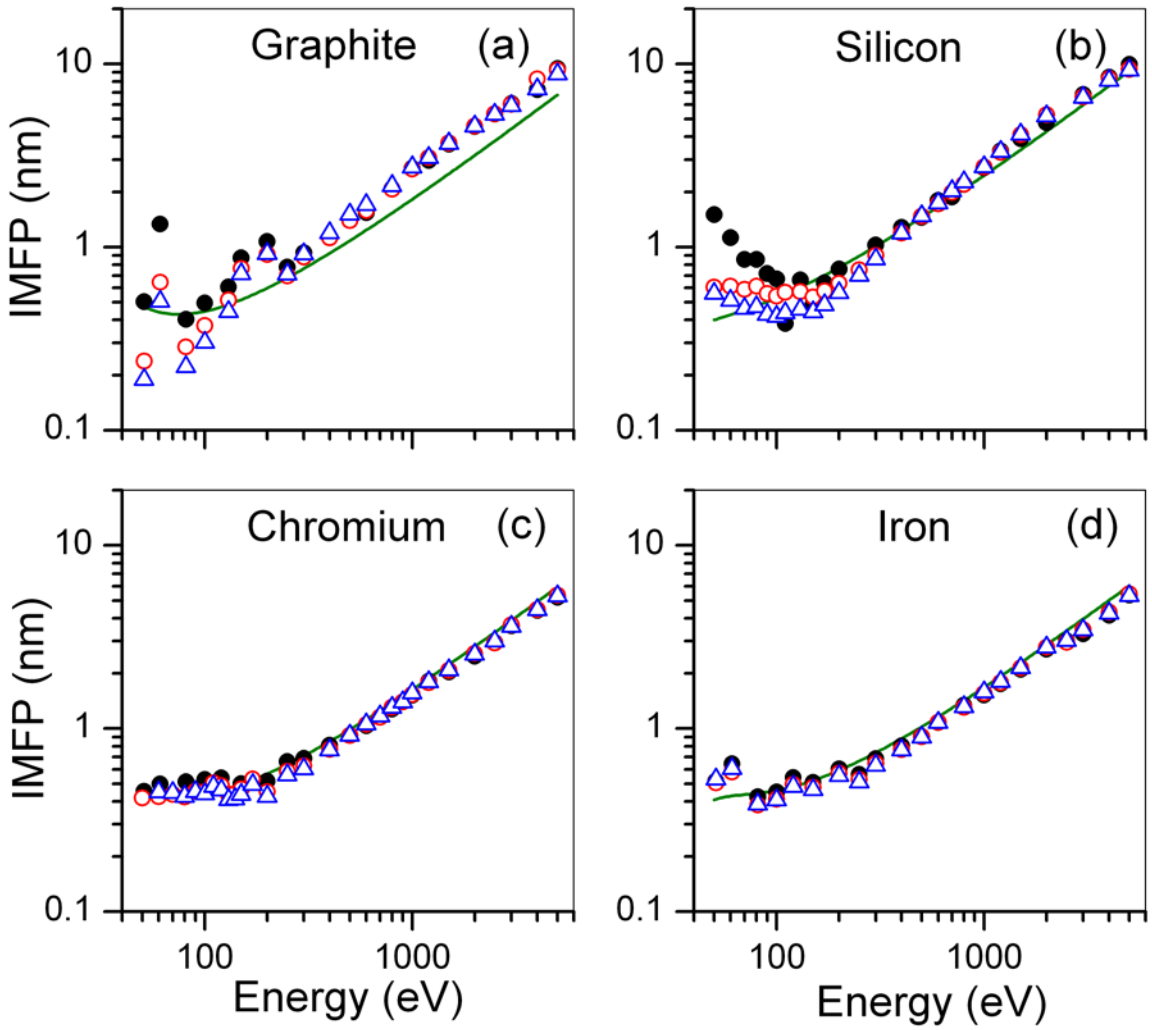

Fig. 17

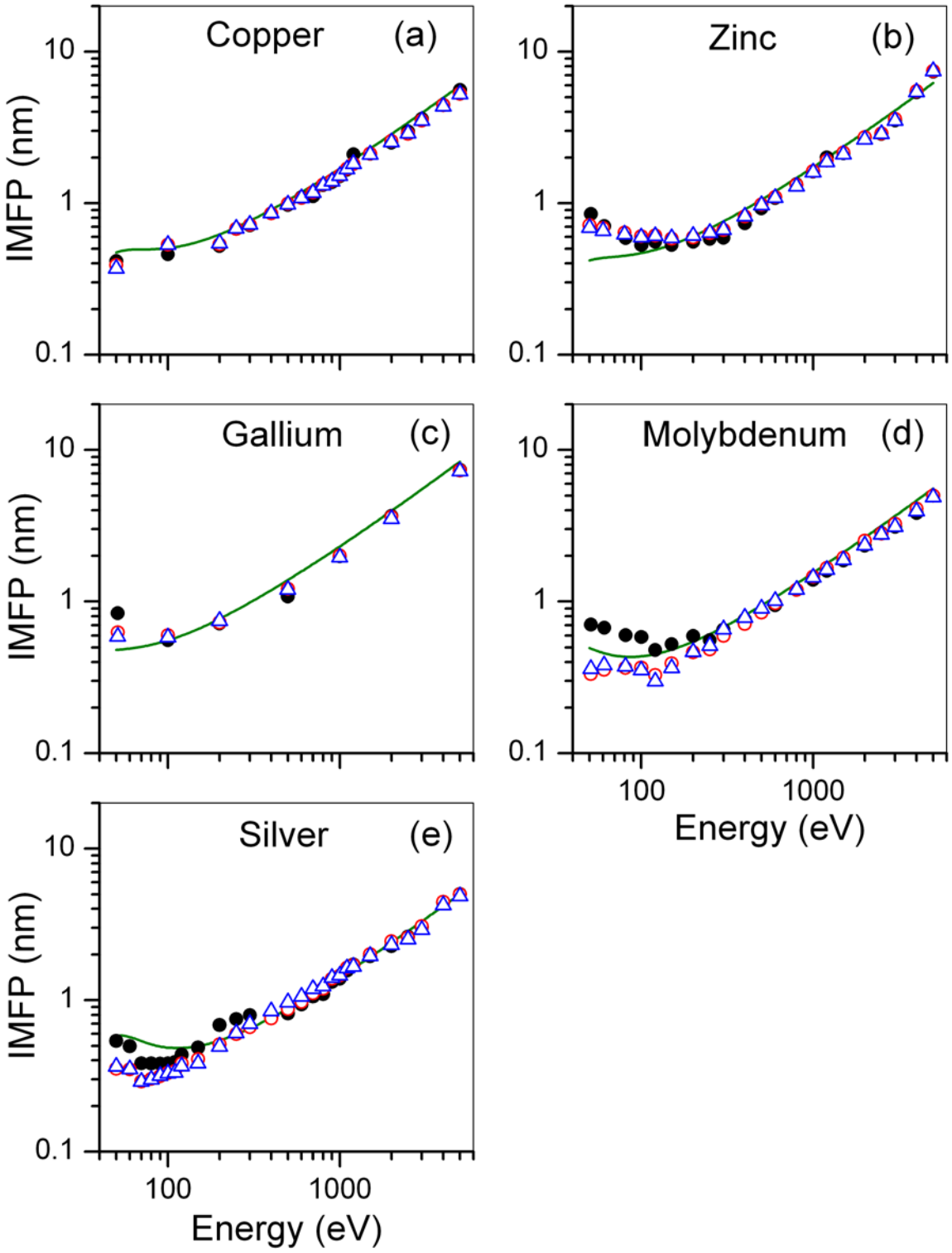

Fig. 18

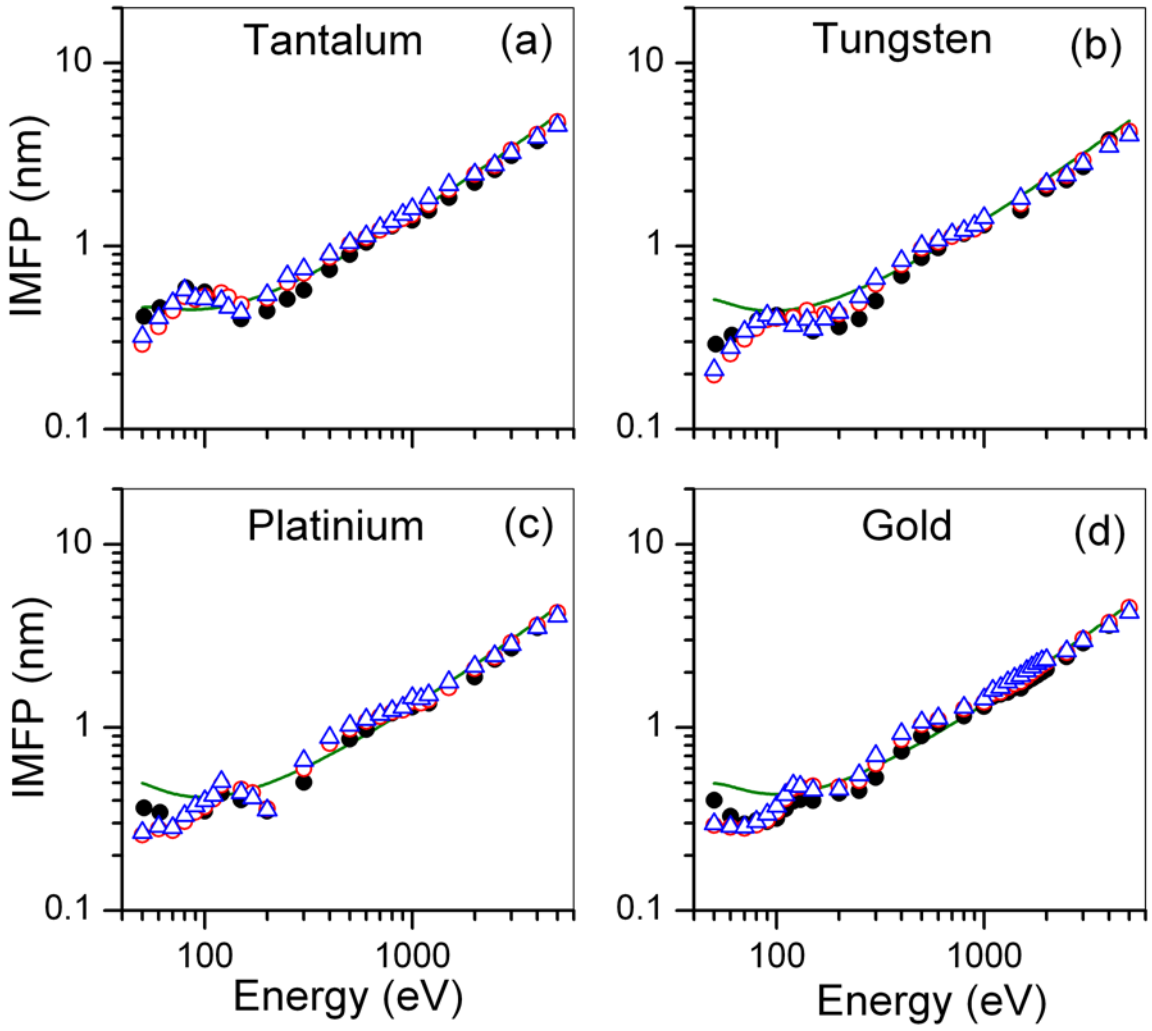

Fig. 19

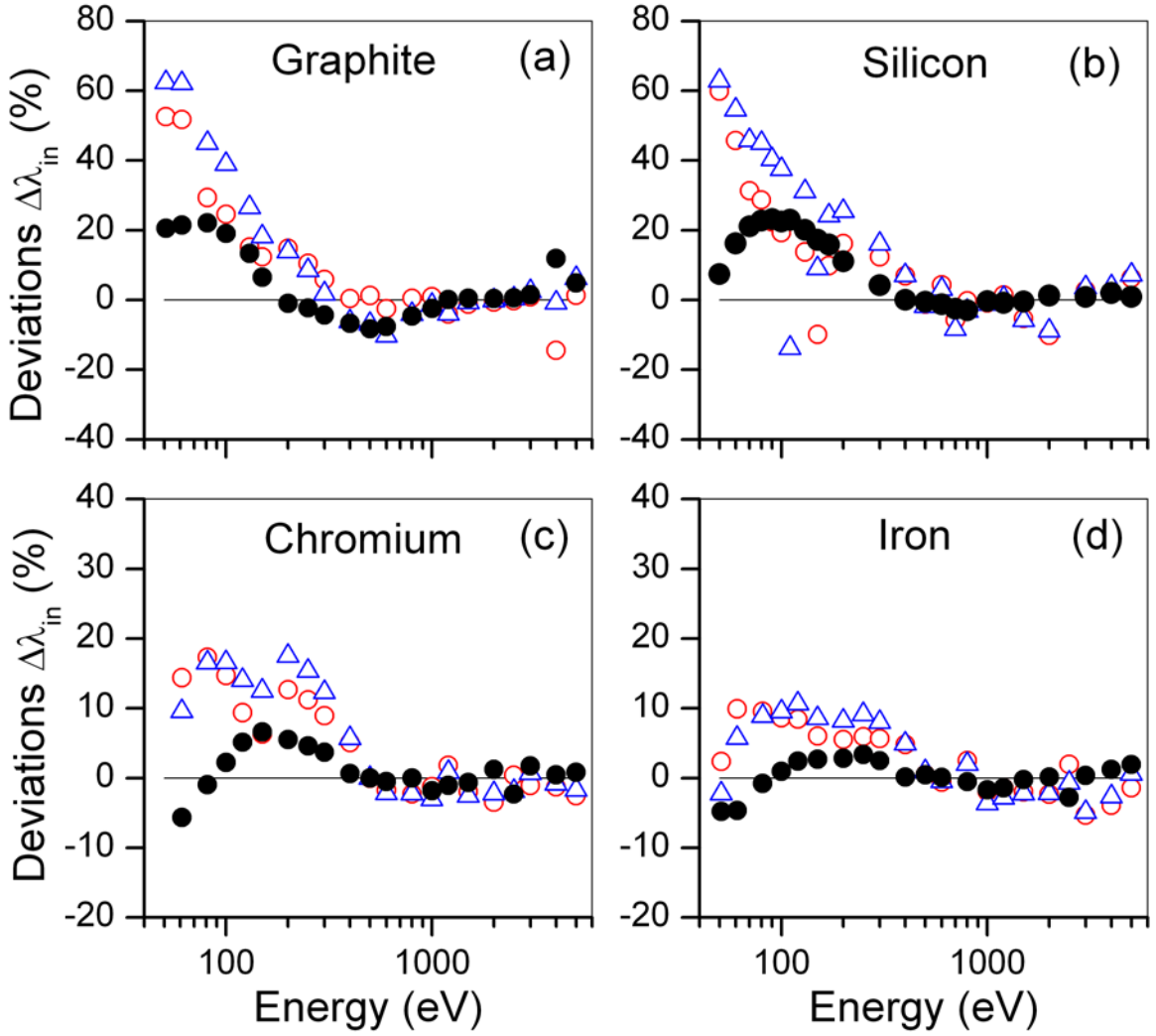

Fig. 20

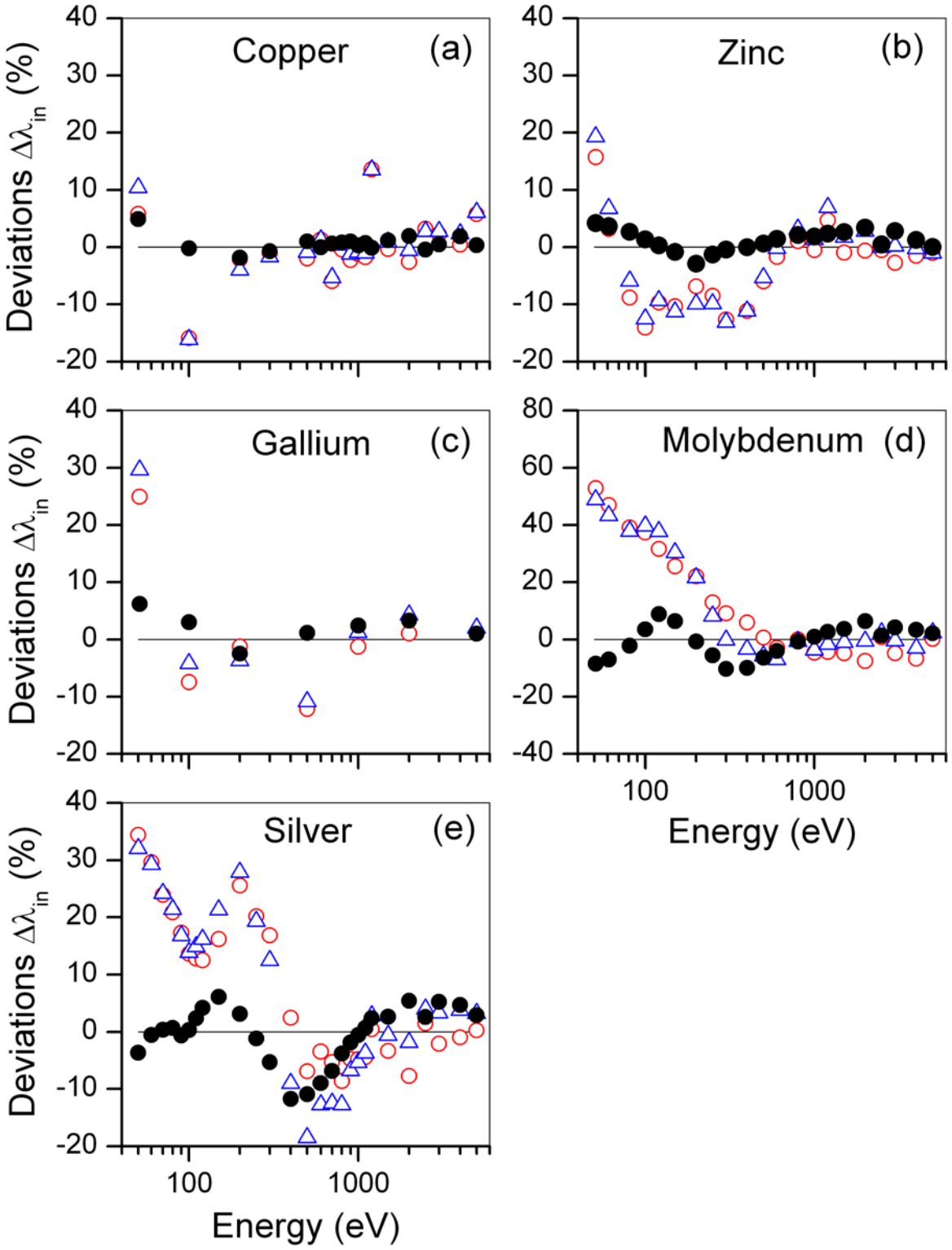

Fig. 21

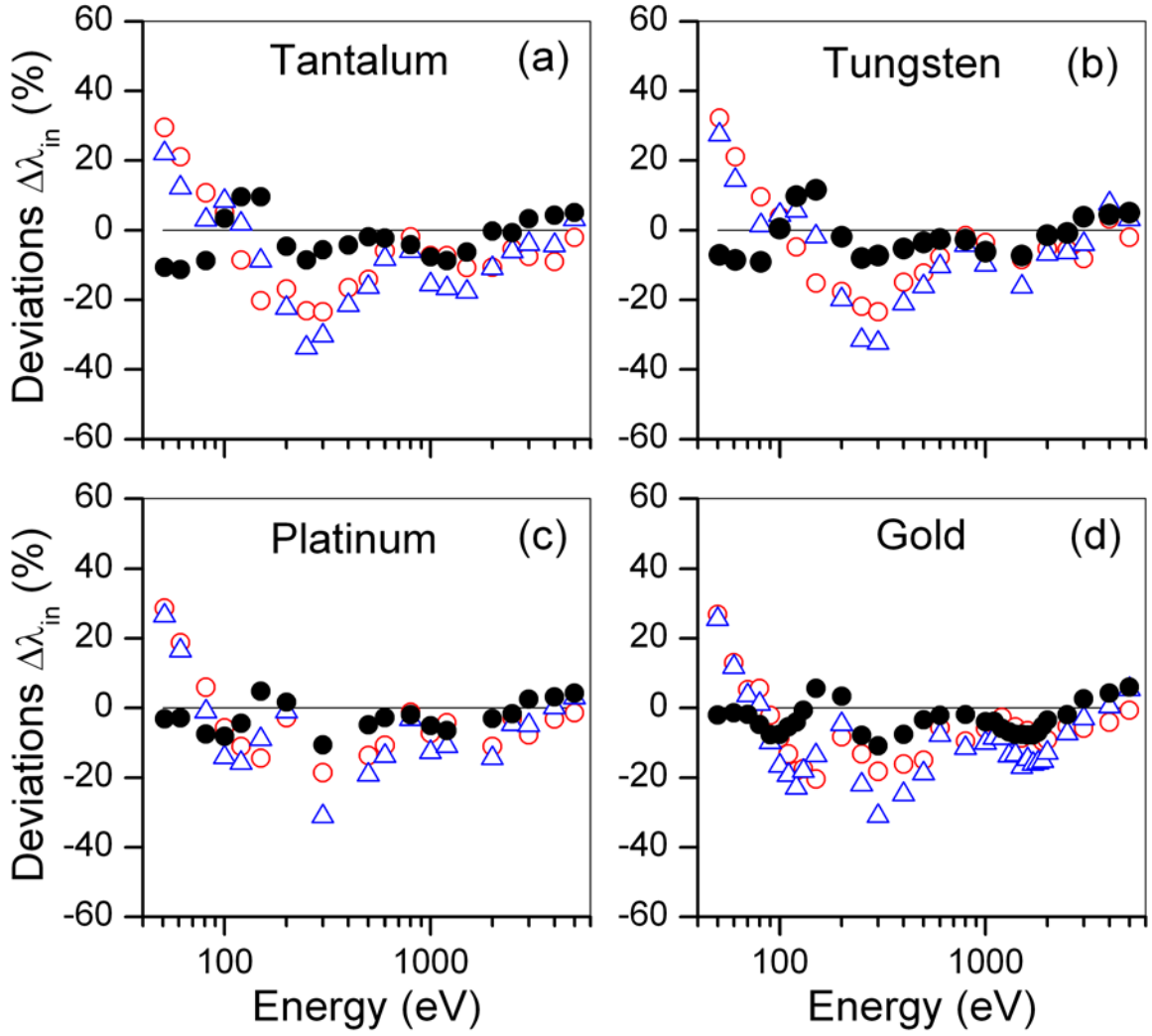

Fig. 22

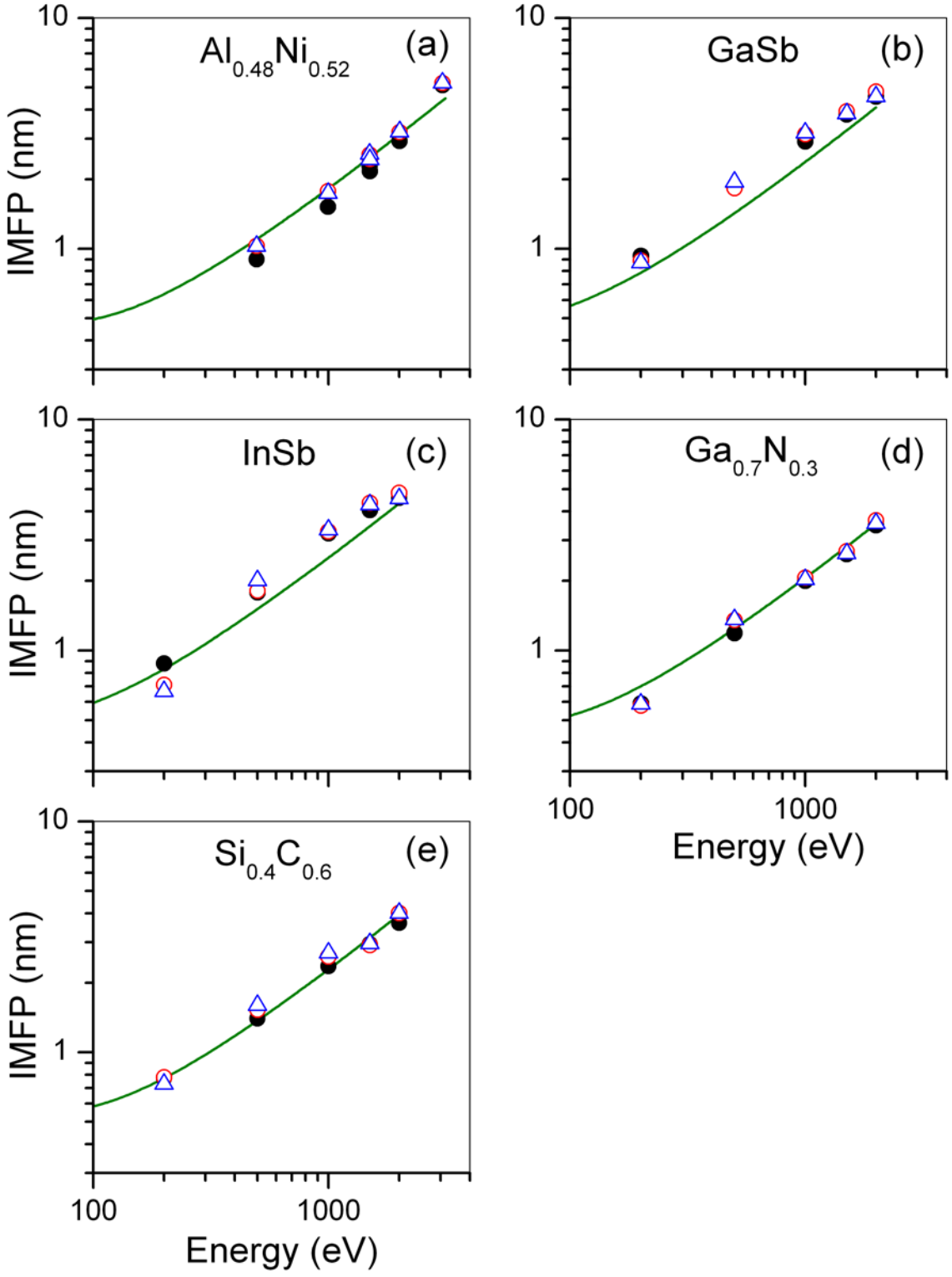

Fig. 23

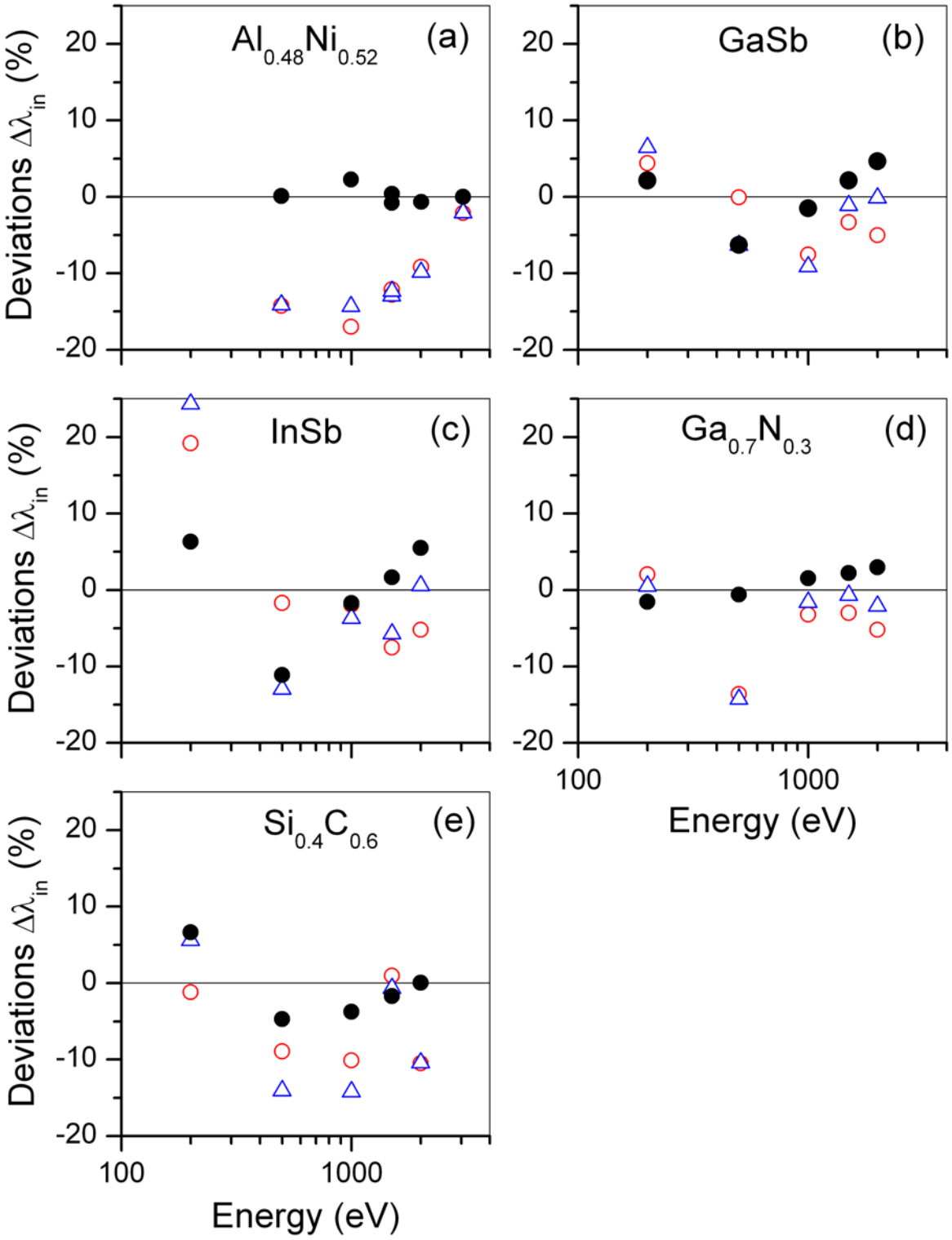

Fig. 24

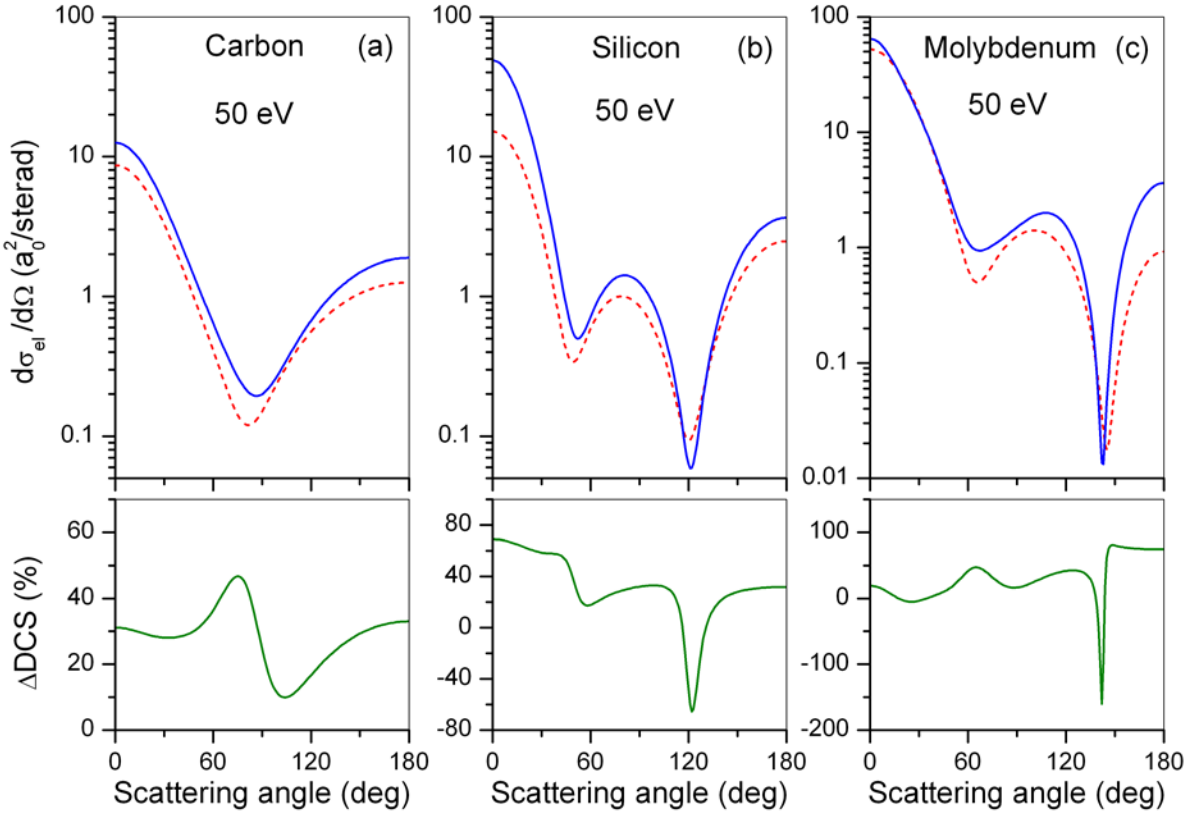

Fig. 25

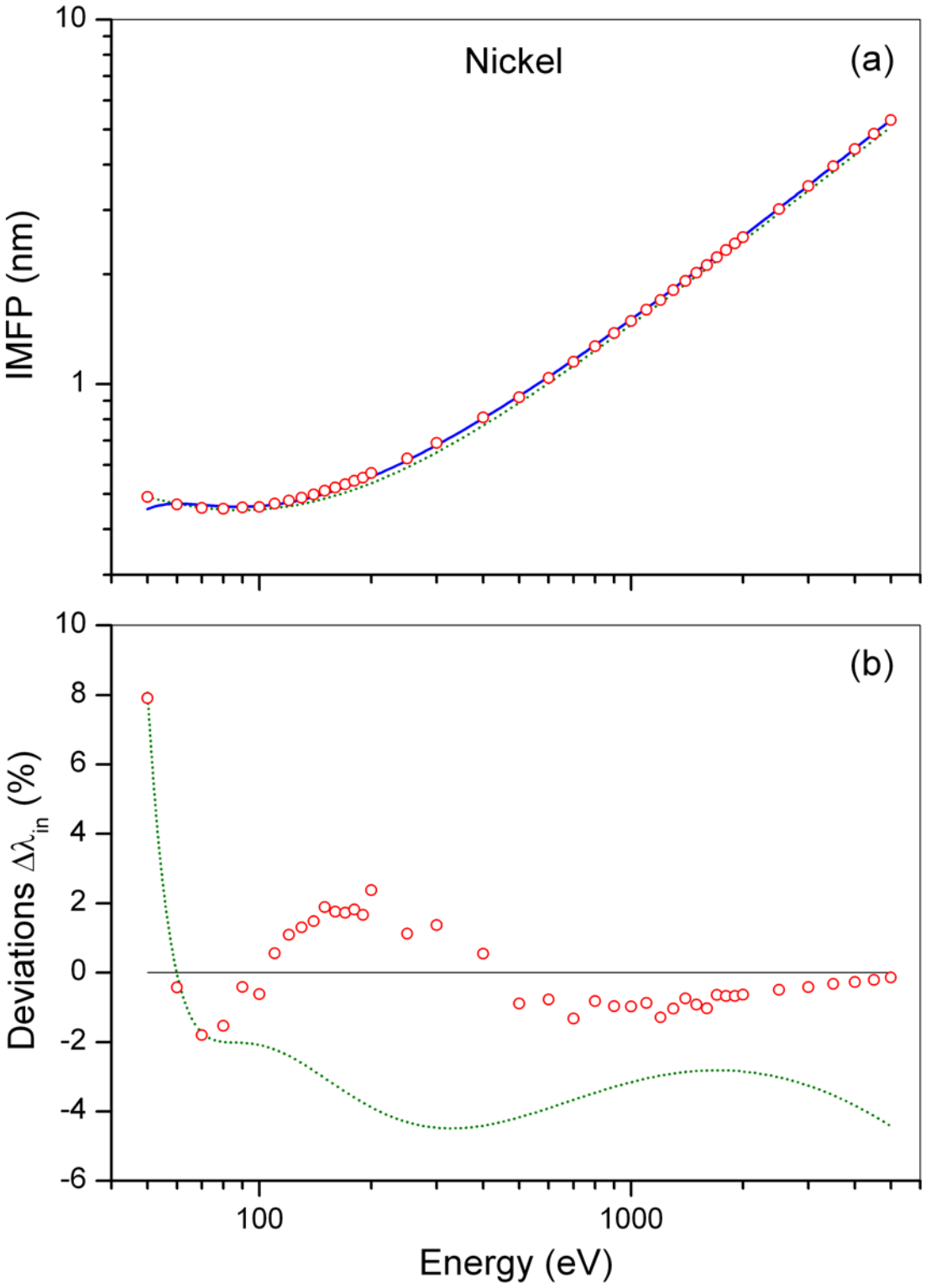

Fig. 26